

# Proximate Tomonaga-Luttinger liquid in a spin-1/2 ferromagnetic XXZ chain compound

Boqiang Li,<sup>1,\*</sup> Xun Chen,<sup>1,\*</sup> Yuqian Zhao,<sup>1,\*</sup> Zhaohua Ma,<sup>1</sup> Zongtang Wan,<sup>1</sup> and Yuesheng Li<sup>1,†</sup>

<sup>1</sup>Wuhan National High Magnetic Field Center and School of Physics,  
Huazhong University of Science and Technology, 430074 Wuhan, China

(Dated: November 12, 2024)

The spin-1/2 ferromagnetic XXZ chain is a prototypical many-body quantum model, exactly solvable via the integrable Bethe ansatz method, hosting a Tomonaga-Luttinger spin liquid. However, its clear experimental realizations remain absent. Here, we present a thorough investigation of the magnetism of the structurally disorder-free compound  $\text{LuCu}(\text{OH})_3\text{SO}_4$ . By conducting magnetization and electron-spin-resonance measurements on the single-crystal sample, we establish that the title compound approximates the spin-1/2 ferromagnetic XXZ chain model with a nearest-neighbor exchange strength of  $J_1 \sim 65$  K and an easy-plane anisotropy of  $\sim 0.994$ . The specific heat demonstrates a distinctive power-law behavior at low magnetic fields (with energy scales  $\leq 0.02J_1$ ) and low temperatures ( $T \leq 0.03J_1$ ). This behavior is consistent with the expectations of the ideal spin-1/2 ferromagnetic XXZ chain model, thereby supporting the formation of a gapless Tomonaga-Luttinger spin liquid in  $\text{LuCu}(\text{OH})_3\text{SO}_4$ .

## I. INTRODUCTION

Spin-1/2 many-body correlated systems can give rise to exotic phases and elementary excitations due to their inherent strong quantum fluctuations and entanglements, capturing significant attention in condensed matter physics and materials science. The exploration, understanding, and control of these exotic phases have been a longstanding goal with promising applications in various fields, including future topological quantum computation [1]. However, achieving this task is exceptionally challenging, stemming from two key aspects: 1. The majority of many-body-correlated quantum systems are too complex to have exact solutions, including eigenstates and eigenvalues. For instance, the ground-state nature of the spin-1/2 kagome-lattice Heisenberg antiferromagnet has been extensively studied for many years but remains elusive [2–5]. 2. Real strongly correlated materials are so complex that their properties cannot be fully captured by simplified theoretical models, particularly in systems with low-lying small-gapped or gapless excitations. The Kitaev model is one of the few exactly solvable spin-1/2 many-body models [6], but its experimental realizations are still under heated debate due to the widespread presence of significant non-Kitaev interactions in real materials [7, 8].

The spin-1/2 XXZ or XXX (Heisenberg) chain, originally proposed by Werner Heisenberg and Hans Bethe, is a prototypical many-body model with eigenstates and eigenvalues that can be exactly solved using the integrable Bethe ansatz method [9, 10]. In the case of a ferromagnetic nearest-neighbor (NN) exchange interaction (strength:  $J_1$ ) and an easy-plane anisotropy ( $0 < \Delta < 1$ ), the model resides deeply within a gapless Tomonaga-Luttinger spin-liquid phase [11, 12]. Numerous candidate compounds for the spin-1/2 ferromagnetic XXZ chain have been previously reported, such as  $\text{LiCuVO}_4$  [13–17],  $\text{LiCuSbO}_4$  [18–20],  $\text{Li}_2\text{ZrCuO}_4$  [21, 22],  $\text{Li}_2\text{CuO}_2$  [23, 24],  $\text{Ca}_2\text{Y}_2\text{Cu}_5\text{O}_{10}$  [25–27],  $\text{CuAs}_2\text{O}_4$  [28],

$\text{PbCuSO}_4(\text{OH})_2$  [29, 30], and others. However, these candidates consistently show substantial next-nearest-neighbor (NNN) antiferromagnetic coupling ( $J_2$ ), comparable to  $J_1$ . Despite their significance as strongly frustrated  $J_1$ - $J_2$  systems, the presence of substantial  $J_2$  typically hinders exact resolution [31]. Furthermore, in the aforementioned Li-based compounds [16, 18, 21] and  $\text{Ca}_2\text{Y}_2\text{Cu}_5\text{O}_{10}$  (Ca/Y disorder) [26], structural disorders are inherent and unavoidable. These disorders can introduce significant complications for many-body modelling, given the apparent interaction randomness [32–36].

Recently, Huangjie Lu et al. reported the successful synthesis of the structurally disorder-free  $\text{Cu}^{2+}$  (spin-1/2) chain compound  $\text{LuCu}(\text{OH})_3\text{SO}_4$ , featuring a crystal size of approximately  $10 \times 25 \times 10 \mu\text{m}$  [37]. However, to the best of our knowledge, its magnetism has not been reported so far. In this study, we implemented a new synthesis method and achieved successful growth of significantly larger single crystals of  $\text{LuCu}(\text{OH})_3\text{SO}_4$ , typically with a size of  $\sim 0.08 \times 1 \times 0.08$  mm. Through magnetization and electron-spin-resonance (ESR) measurements on the single-crystal sample, we determined the detailed spin Hamiltonian. Our findings indicate that both interchain and next-nearest-neighbor intrachain couplings are less significant,  $J_{p1}/J_1 \sim 1.01\%$ ,  $J_{p2}/J_1 \sim -0.18\%$ , and  $J_2/J_1 \sim 1\%$  (see Fig. 1).  $\text{LuCu}(\text{OH})_3\text{SO}_4$  closely approximates the ideal spin-1/2 ferromagnetic XXZ chain model with  $J_1 \sim 65$  K and  $\Delta \sim 0.994$ . The specific heat and magnetization measurements down to  $T = 35$  mK ( $\sim 0.0005J_1$ ) are consistent with the expectations of the ideal model, supporting the emergence of a gapless Tomonaga-Luttinger spin liquid in  $\text{LuCu}(\text{OH})_3\text{SO}_4$ .

## II. METHODS

### A. Sample synthesis

The microcrystals of  $\text{LuCu}(\text{OH})_3\text{SO}_4$  were synthesized using the traditional hydrothermal method as reported in Ref. [37], resulting in crystals of approximately  $5 \times 30 \times 5 \mu\text{m}$

\* These authors contributed equally to this work

† yuesheng\_li@hust.edu.cn

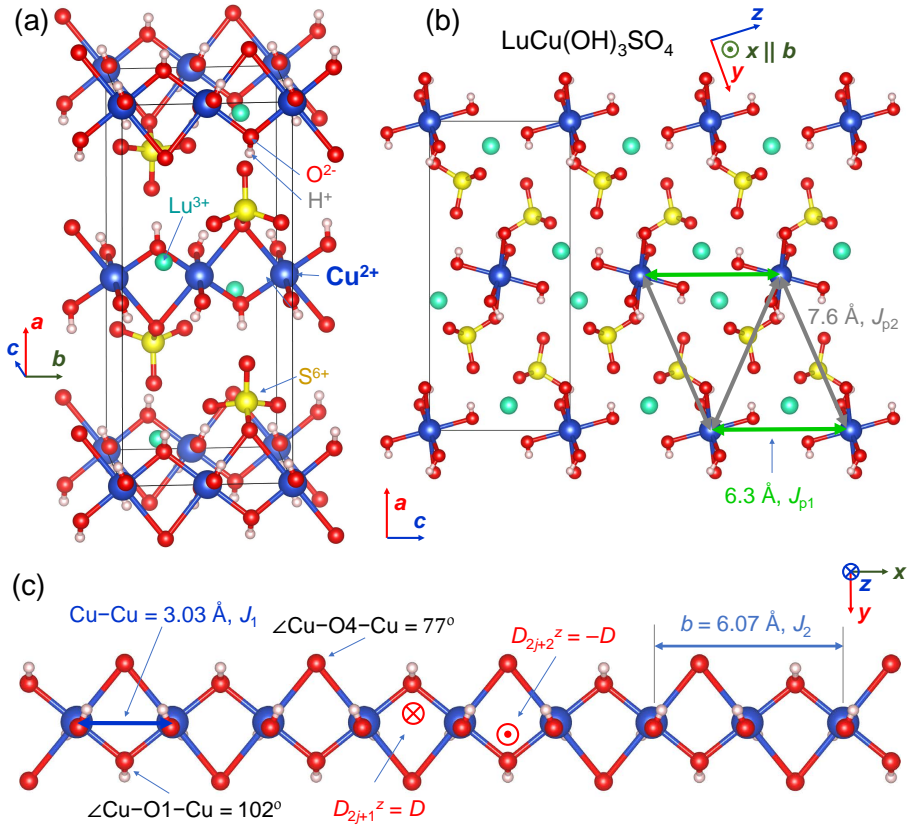


FIG. 1. (a) Crystal structure of  $\text{LuCu}(\text{OH})_3\text{SO}_4$ . (b) View along the spin chain ( $b$  axis) of the crystal structure. (c)  $\text{CuO}_2$  chain viewed along the  $z$  axis. Dominant nearest-neighbor (NN) ferromagnetic exchange ( $J_1$ ) and weaker couplings beyond first neighbors ( $J_2$ ,  $J_{p1}$ , and  $J_{p2}$ ) are displayed in (b) and (c). NN Dzyaloshinsky-Moriya interaction vectors are shown in (c). The local  $xyz$ -coordinate system for spin components is defined, and thin black lines mark the unit cells.

in size. To enhance crystal size, we employed copper plates ( $\text{Cu} \geq 99.99\%$ ) as the Cu source to slow down the chemical reaction. This modification successfully increased the crystal size to  $\sim 0.08 \times 1 \times 0.08$  mm [38]. The high quality and phase purity of our samples were confirmed through both powder and single-crystal XRD measurements. The longest dimension of the crystal aligns with the  $b$  axis, and approximately 800 of the largest single crystals, totaling  $\sim 10$  mg, are aligned along the  $b$  axis using GE varnish for magnetic property measurements. We are only able to align the crystals along the  $b$  axis due to the small dimensions that make distinguishing non- $b$  directions challenging.

## B. Sample characterizations

The ESR spectra were obtained using a continuous-wave spectrometer (Bruker EMXmicro-6/1) at x-band frequencies ( $\sim 9.8$  GHz) for both single-crystal and powder samples ( $\sim 10$  mg). Magnetization and dc/ac susceptibilities of  $\text{LuCu}(\text{OH})_3\text{SO}_4$  (up to 7 T, down to 1.8 K) were measured in a magnetic property measurement system (Quantum Design) using powder samples ( $\sim 38$  mg, ground from single crystals)

and well-aligned single-crystal samples ( $\sim 10$  mg) along the  $b$  axis. The powder sample (6.95 mg) was utilized for magnetization measurements at between 0.035 and 1.8 K, employing a Faraday force magnetometer within a  $^3\text{He}$ - $^4\text{He}$  dilution refrigerator (KELMX-400, Oxford Instruments). Superconducting coils (in INTA-LLD-S12/14, Oxford Instruments) generated the main magnetic fields and field gradients ( $dH/dl = \pm 10$  T/m), and electrical capacitance was measured using a digital capacitance bridge (AH-2500A, Andeen-Hagerling, Inc.) with the three-terminal method [39, 40].

The specific heat measurements, down to 1.8 K, were performed in a Physical Properties Measurement System (Quantum Design) using dry-pressed disks of the powders (4.86 mg). N grease was used to facilitate thermal contact between the power sample and the puck, and the sample coupling was measured to be better than 95%. The specific-heat contributions of the N grease and puck were initially measured and subtracted from the data. Specific heat measurements between 0.1 and 1.8 K were carried out using a thermal relaxation method in the dilution refrigerator, utilizing a powder sample weighing 2.61 mg. The thermal link to the bath was established using a bronze wire of appropriate diameter and length to achieve quasiadiabatic conditions [34, 41]. A  $\sim 10$  nm NiCr layer was deposited on one side of the platform and

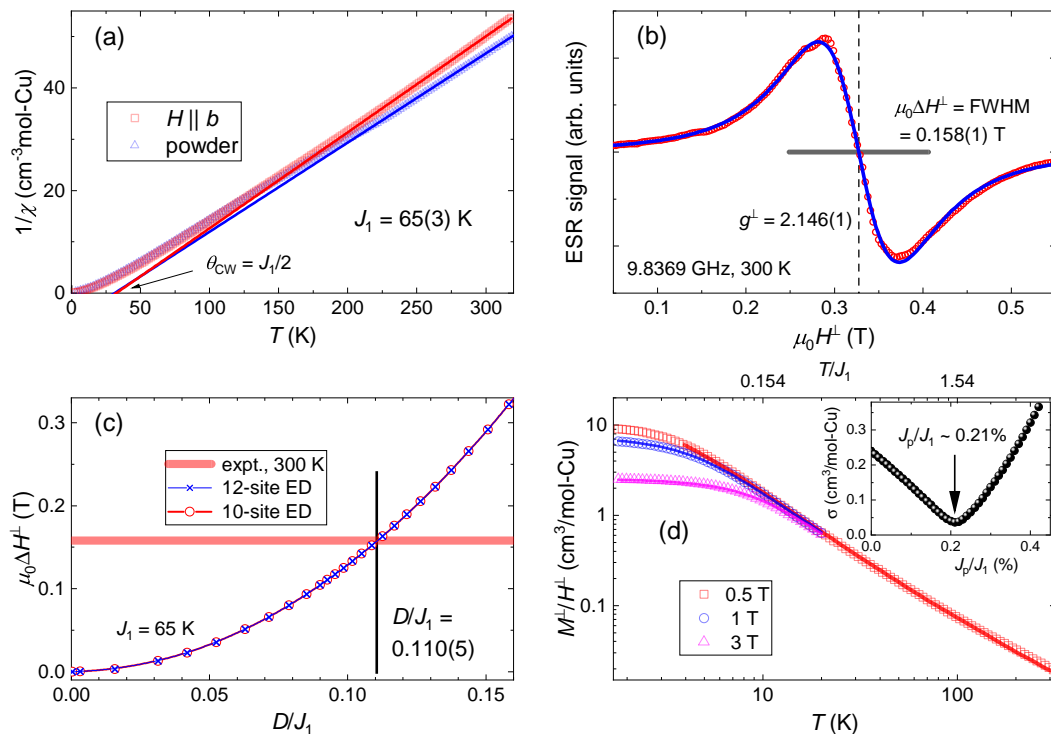


FIG. 2. Determining couplings  $J_1$ ,  $D$ , and  $J_p \equiv J_{p1}/3 + 2J_{p2}/3$ . (a) Inverse magnetic susceptibilities measured on single-crystal and powder samples, with Curie-Weiss fits (lines) above 200 K. (b) Electron spin resonance (ESR) spectrum measured along the  $b$  axis ( $H^\perp$ ) on the single-crystal sample at 300 K. The blue line represents the fit using the derivative Lorentzian function, with resonance field ( $g^\perp = 2.146$ ) and full width at half maximum (FWHM =  $\mu_0 \Delta H^\perp$ ) marked. (c) Dzyaloshinsky-Moriya (DM) strength ( $D$ ) dependence of  $\mu_0 \Delta H^\perp$ , calculated using exact diagonalization (ED) with  $J_1 = 65$  K and at  $T = 300$  K. The determined DM anisotropic strength is  $D/J_1 = 0.110(5)$ . (d) Magnetization measured on the single-crystal sample with magnetic fields along the  $b$  axis, with stochastic series expansion (SSE) calculations (lines) shown using least-square parameters. Inset: Standard deviation  $\sigma$  as a function of  $J_p/J_1$  calculated using the experimental data between 1.8 and 20 K at  $\mu_0 H^\perp = 1$  and 3 T. The arrow denotes the optimal parameter  $J_p/J_1 = 0.21(1)\%$ . Periodic boundary conditions are used in both ED and SSE computations.

served as a heater (resistance  $\sim 10$  k $\Omega$ ). The chip thermometer (CX-1010-BR, LakeShore) was *in situ* calibrated against a reference thermometer (RX-102B-RS-0.02B, LakeShore, calibrated down to 20 mK) at each applied magnetic field by turning off the heater.

### C. Numerical methods

We utilized finite-size ( $N \leq 28$ ) ED, large-scale ( $N = 100$ ) stochastic series expansion (SSE), and integrable Bethe ansatz ( $N \rightarrow \infty$ ) methods to thoroughly investigate the strongly correlated quantum magnetism of LuCu(OH)<sub>3</sub>SO<sub>4</sub>. In the Bethe simulations, we employed  $\Delta = \cos(\pi/29)$  ( $\sim 0.994$ ). Detailed discussions on the validation, consistency, and finite-size effects of these three methods are provided in Supplementary material [38].

## III. RESULTS AND DISCUSSIONS

### A. Crystal structure and symmetry analysis

Figure 1 displays the crystal structure of LuCu(OH)<sub>3</sub>SO<sub>4</sub> refined using single-crystal x-ray diffraction (XRD) data [38]. Due to significant differences among Cu<sup>2+</sup>, Lu<sup>3+</sup>, OH<sup>-</sup>, and SO<sub>4</sub><sup>2-</sup>, the occurrence of site-mixing structural disorder is expected to be prohibited. Firstly, our XRD data, measured on both powder and single-crystal samples [38], indeed show no clear evidence of structural disorder, aligning with previously reported results [37]. Secondly, the single-crystal ESR spectrum, highly sensitive to quasi-free magnetic moments induced by structural disorder and interaction randomness [42], does not exhibit any sharp components (linewidth  $< 0.02$  T) with hyperfine structures [see Fig. 2(b)]. Lastly, the single-crystal magnetization can be well reproduced by the *ab-initio* model down to  $\sim 1.8$  K ( $\mu_0 H^\perp \geq 1$  T) without considering structural disorder [see Fig. 2(d)]. Therefore, we propose LuCu(OH)<sub>3</sub>SO<sub>4</sub> as a structurally disorder-free compound for the study of strongly correlated quantum magnetism.

The superexchange coupling ( $J_1$ ) between the NN Cu<sup>2+</sup>

ions, with Cu-Cu distance  $b/2 = 3.03 \text{ \AA}$ , is mediated by  $\text{O}^{2-}$  and  $\text{O}4^{2-}$  along the spin-1/2 chain, with  $|\text{Cu-O}1| \sim 1.95 \text{ \AA}$  &  $\angle\text{Cu-O}1\text{-Cu} \sim 102^\circ$  and  $|\text{Cu-O}4| \sim 2.44 \text{ \AA}$  &  $\angle\text{Cu-O}4\text{-Cu} \sim 77^\circ$  (see Fig. 1). When the Cu-O-Cu bond angle exceeds the critical value of  $\varphi_c \sim 96^\circ$ , the exchange interaction tends to be antiferromagnetic (AF). Conversely, a ferromagnetic (FM) exchange interaction is expected when the bond angle is smaller. In  $\text{LuCu}(\text{OH})_3\text{SO}_4$ , the superexchanges along the Cu-O1-Cu (AF) and Cu-O4-Cu (FM) paths may compete. Given that  $\varphi_c - \angle\text{Cu-O}4\text{-Cu} \sim 19^\circ$  exceeds  $\angle\text{Cu-O}1\text{-Cu} - \varphi_c \sim 6^\circ$ , we find the detection of a ferromagnetic nature in  $J_1$  [Fig. 2(a)] within  $\text{LuCu}(\text{OH})_3\text{SO}_4$  to be unsurprising.

Magnetic chains are well spatially separated by non-magnetic  $\text{Lu}^{3+}$  and  $\text{SO}_4^{2-}$  with much larger distances of  $6.3 \text{ \AA}$  along the  $J_{p1}$  path and  $7.6 \text{ \AA}$  along the  $J_{p2}$  path [see Fig. 1(b)], respectively. This suggests the quasi-one-dimensional nature of the spin system in  $\text{LuCu}(\text{OH})_3\text{SO}_4$ . Our density functional theory (DFT)+ $U$  calculations for  $\text{LuCu}(\text{OH})_3\text{SO}_4$  semi-quantitatively demonstrate that  $J_1 \sim 50 \text{ K}$  is ferromagnetic, with  $J_{p1}/J_1 \sim 4.8\%$ ,  $J_{p2}/J_1 \sim 0.1\%$ , and  $J_2/J_1 \sim 1.0\%$  [38]. These results indicate that the spin system of  $\text{LuCu}(\text{OH})_3\text{SO}_4$  closely approximates the ideal spin-1/2 ferromagnetic chain model.

In  $\text{Cu}^{2+}$ -based magnets, the NN exchange coupling is typically isotropic and symmetric (Heisenberg). In addition to the isotropic NN coupling, the antisymmetric Dzyaloshinsky-Moriya (DM) interaction tends to be dominant, arising from spin-orbit coupling if allowed by symmetry [43, 44]. Similar to other  $\text{Cu}^{2+}$ -based magnets, such as  $\text{ZnCu}_3(\text{OH})_6\text{Cl}_2$  [44] and  $\text{YCu}_3(\text{OH})_{6.5}\text{Br}_{2.5}$  [42], we find, through a standard symmetry analysis, that the nearly Heisenberg Hamiltonian invariant under the  $Pnma$  space group symmetry of  $\text{LuCu}(\text{OH})_3\text{SO}_4$  [see Fig. 1(c)] is given by,

$$\mathcal{H} = -J_1 \sum_j \mathbf{S}_j \cdot \mathbf{S}_{j+1} + D \sum_j (-1)^{j+1} (S_j^x S_{j+1}^y - S_j^y S_{j+1}^x) + \mathcal{H}', \quad (1)$$

where  $\mathcal{H}' = J_2 \sum_j \mathbf{S}_j \cdot \mathbf{S}_{j+2} + J_{p1} \sum_{\langle j, j_{p1} \rangle} \mathbf{S}_j \cdot \mathbf{S}_{j_{p1}} + J_{p2} \sum_{\langle j, j_{p2} \rangle} \mathbf{S}_j \cdot \mathbf{S}_{j_{p2}} + \dots$  represents interactions beyond the nearest neighbors. The periodic boundary condition,  $\mathbf{S}_j \equiv \mathbf{S}_{j+N}$ , is considered, where  $N$  is an even [45] number of spins (i.e., spin length). Since inversion centers are located at any  $\text{Cu}^{2+}$  ions, the NNN DM interaction is symmetrically forbidden. The parameter  $D$  in Equation (1) denotes the strength of the NN DM interaction, and its sign does not affect the resulting observables due to symmetry. Therefore, for consistency, we set  $D > 0$  throughout this work. Additionally, the superscripts, “ $\perp$ ” and “ $\parallel$ ”, denote the quantity with the applied magnetic field perpendicular and parallel to the  $z$  axis of the spin model [see Fig. 1(c)], respectively, throughout this work.

Above  $\sim 200 \text{ K}$ , the inverse magnetic susceptibilities ( $\chi$ ) of  $\text{LuCu}(\text{OH})_3\text{SO}_4$  exhibit a linear  $T$ -dependence, following the Curie-Weiss (CW) law,  $\chi = C/(T - \theta_{\text{CW}})$  [see Fig. 2(a)]. Through CW fits, we obtain the  $g$  factor as  $g = \sqrt{4k_B C / (\mu_0 N_A \mu_B^2)}$ . The resulting values are  $g^\perp \sim 2.13$  and  $g^{\text{powder}} \sim 2.2$ , based on magnetic susceptibilities measured on the single-crystal and powder samples, respectively. These

values are roughly consistent with the ESR [see Fig. 2(b)] and magnetization data. Additionally, the NN ferromagnetic couplings are fitted to be  $J_1 = 2\theta_{\text{CW}} = 64.9 \pm 0.7$  and  $62.3 \pm 0.6 \text{ K}$  for the single-crystal and powder samples, respectively [Fig. 2(a)]. Thus, we conclude the ferromagnetic  $J_1 = 65(3) \text{ K}$  for  $\text{LuCu}(\text{OH})_3\text{SO}_4$ .

## B. Electron spin resonance spectrum

Figure 2(b) displays the x-band ESR spectrum measured on the single-crystal sample of  $\text{LuCu}(\text{OH})_3\text{SO}_4$  with the magnetic field applied along the  $b$  axis. The experimental data are well-fitted using the first derivative Lorentzian function [see Fig. 2(b)] [46], revealing a sizable linewidth of  $\mu_0 \Delta H^\perp = 0.158(1) \text{ T}$ . Below, we discuss various sources contributing to the broadening of the ESR signal in the high- $T$  limit.

Firstly, the hyperfine interaction contributes to the ESR linewidth as  $\mu_0 \Delta H_h \sim |A_h|^2 / (g\mu_B J_1) < 0.01 \text{ mT}$ , where  $|A_h| < 500 \text{ MHz}$  is the hyperfine coupling between  $\text{Cu}^{2+}$  electronic and nuclear spins [47]. Secondly, the dipole-dipole magnetic interaction also broadens the signal by  $\mu_0 \Delta H_d \sim |E_d|^2 / (g\mu_B J_1) \sim 0.09 \text{ mT}$ . Here,  $|E_d| \sim 2\mu_0 g^2 \mu_B^2 / (\pi b^3) \sim 1.9 \text{ GHz}$  represents the strength of the dipole-dipole interaction, and  $b/2$  is the NN Cu-Cu distance [see Fig. 1(c)]. Thirdly, as there is only one Wyckoff position for  $\text{Cu}^{2+}$  ions, the uniform Zeeman interaction cannot broaden the single-crystal ESR signal [44, 46, 48]. Even when all the above contributions are considered together, they are more than two orders of magnitude smaller than the observed linewidth. Therefore, in the high- $T$  limit ( $T \sim 300 \text{ K}$ ), the exchange anisotropy of the DM interaction predominantly accounts for the observed ESR linewidth in  $\text{LuCu}(\text{OH})_3\text{SO}_4$ , with  $\mu_0 \Delta H^\perp \sim D^2 / (g\mu_B J_1)$  and  $D/J_1 \sim 0.1$ , similar to several other  $\text{Cu}^{2+}$ -based magnets [44].

To determine  $D$  precisely, we conduct detailed many-body calculations for the transverse ESR linewidth measured at  $300 \text{ K}$  using  $\mu_0 \Delta H^\perp = \sqrt{2\pi} (M_2^x)^3 / M_4^x / (g^\perp \mu_B)$ . Here,  $M_2^x = \langle [\mathcal{H}_{\text{DM}}^x, M^+] [M^-, \mathcal{H}_{\text{DM}}^x] \rangle / \langle M^+ M^- \rangle$  and  $M_4^x = \langle [\mathcal{H}^x, [\mathcal{H}_{\text{DM}}^x, M^+]] [\mathcal{H}^x, [\mathcal{H}_{\text{DM}}^x, M^-]] \rangle / \langle M^+ M^- \rangle$  are the second and fourth moments, respectively [49]. In these expressions, we set  $\mathcal{H}_{\text{DM}}^x = D \sum_j (-1)^{j+1} (S_j^y S_{j+1}^z - S_j^z S_{j+1}^y)$ ,  $\mathcal{H}^x = -J_1 \sum_j \mathbf{S}_j \cdot \mathbf{S}_{j+1} + \mathcal{H}_{\text{DM}}^x - \mu_0 H^\perp g^\perp \sum_j S_j^z$ ,  $M^\pm \equiv \sum_j S_j^x \pm i S_j^y$ , and  $\langle \rangle$  represents the equilibrium thermal average,  $\langle O \rangle = \text{Tr}(O e^{-\beta \mathcal{H}^x}) / \text{Tr}(e^{-\beta \mathcal{H}^x})$  where  $\beta \equiv 1/(k_B T)$ . At a high temperature of  $T = 300 \text{ K}$  ( $\sim 4.6 J_1$ ), the calculated  $\mu_0 \Delta H^\perp$  shows no evident finite-size effect and is a monotone increasing function of  $D/J_1$ , as shown in Fig. 2(c). By comparing with the experimental ESR linewidth, we conclude  $D/J_1 = 0.110(5)$  for  $\text{LuCu}(\text{OH})_3\text{SO}_4$ . Furthermore, the observed  $g$ -factor shift from the free electron value  $g_e = 2.0023$ ,  $(g^\perp - g_e)/g_e \sim 0.072$  ( $\sim D/J_1$ ) [43], also supports the above conclusion.

In comparison, the main ESR signal of the powder sample is broader,  $\mu_0 \Delta H_{\text{powder}} \sim 0.36 \text{ T}$  [38]. The ESR linewidth calculated along the  $z$  axis is two times larger than the transverse one,  $\mu_0 \Delta H^\parallel \sim 2\mu_0 \Delta H^\perp$ , which partially accounts for

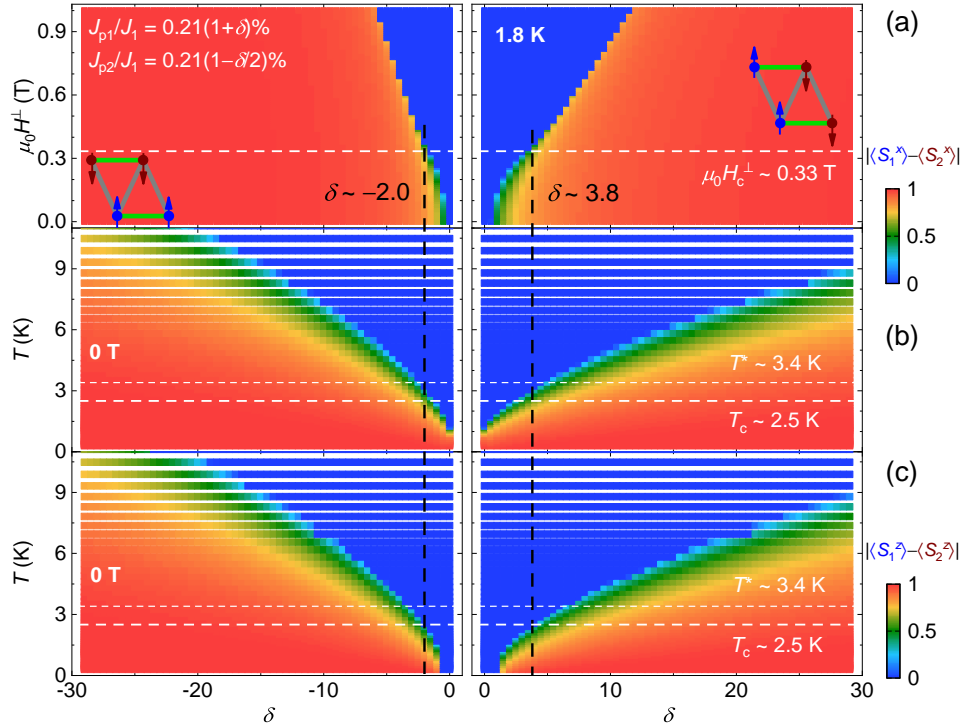


FIG. 3. Interchain antiferromagnetic order parameters calculated using the SSE method with a self-consistent mean-field treatment of interchain interactions. (a)  $|\langle S_1^x \rangle - \langle S_2^x \rangle|$  at 1.8 K. (b)  $|\langle S_1^x \rangle - \langle S_2^z \rangle|$  at 0 T. (c)  $|\langle S_1^z \rangle - \langle S_2^z \rangle|$  at 0 T. The normalized interchain couplings are given as  $J_{p1}/J_1 = (1+\delta)J_p/J_1$  and  $J_{p2}/J_1 = (1-\delta/2)J_p/J_1$ , where  $J_p/J_1 = 0.21\%$  (antiferromagnetic) is fixed (refer to Fig. 2). At  $\delta > 0$ , the dominant antiferromagnetic  $J_{p1}$  induces interchain stripe-I order along  $J_{p1}$  (along green bonds, see right inset of a), whereas at  $\delta < 0$ , the dominant antiferromagnetic  $J_{p2}$  causes stripe-II order along  $J_{p2}$  (along grey bonds, see left inset of a). The critical field of  $\mu_0 H_c^\perp \sim 0.33$  T (dashed white line in a) and critical temperature of  $T_c \sim 2.5$  K are obtained from the field and temperature dependence of susceptibility measured at  $T = 1.8$  K and  $H^\perp \rightarrow 0$ , respectively, on the single-crystal sample (refer to Fig. 4).  $T^*$  denotes the temperature at which interchain magnetic ordering starts [Fig. 4(d)].

the larger value of  $\mu_0 \Delta H_{\text{powder}}$ . On the other hand, the anisotropy of the  $g$ -factor tensor should further explain the observed  $\mu_0 \Delta H_{\text{powder}}$  in  $\text{LuCu}(\text{OH})_3\text{SO}_4$ .

### C. Ferromagnetic XXZ chain model

The original spin Hamiltonian of  $\text{LuCu}(\text{OH})_3\text{SO}_4$  [Eq. (1)] includes the NN antisymmetric DM interaction, significantly increasing the computational cost and making low- $T$  simulations challenging. Therefore, we introduce a unitary transformation operator,

$$\mathcal{T}_u = \exp(i \sum_j \phi_j S_j^z), \quad (2)$$

where  $\phi_j = \arctan(D/J_1)[1 - (-1)^{j+1}]/2$ . Through a canonical transformation,  $\tilde{\mathcal{H}} = \mathcal{T}_u^\dagger \mathcal{H} \mathcal{T}_u$  [50], we obtain a spin-1/2

ferromagnetic XXZ chain,

$$\tilde{\mathcal{H}} = -\sqrt{J_1^2 + D^2} \sum_j (S_j^x S_{j+1}^x + S_j^y S_{j+1}^y + \Delta S_j^z S_{j+1}^z) + \mathcal{H}', \quad (3)$$

where  $\Delta = J_1/\sqrt{J_1^2 + D^2} = 0.994$  shows an easy-plane anisotropy for  $\text{LuCu}(\text{OH})_3\text{SO}_4$ . Since the unitary transformation doesn't change the trace, one can calculate the observable by  $\langle O \rangle = \text{Tr}(O e^{-\beta \tilde{\mathcal{H}}})/\text{Tr}(e^{-\beta \tilde{\mathcal{H}}}) = \text{Tr}(\tilde{O} e^{-\beta \mathcal{H}})/\text{Tr}(e^{-\beta \mathcal{H}})$ , where  $\tilde{O} = \mathcal{T}_u^\dagger O \mathcal{T}_u$ . We confirmed the equivalence between Equations (1) and (3) through finite-size exact diagonalization (ED) calculations.

When a magnetic field is applied along the  $z$  axis, the Zeeman term remains invariant under  $\mathcal{T}_u$ ,  $\mathcal{H}_Z^\parallel \equiv \mathcal{H}_Z^\parallel$ , and thus we can efficiently utilize the ferromagnetic XXZ chain model expressed in Eq. (3) along with  $\mathcal{H}_Z^\parallel$  to calculate observables. In cases where the magnetic field is applied perpendicular to the  $z$  axis, such as along the  $b$  axis, the Zeeman term is no longer invariant under  $\mathcal{T}_u$ , leading to expensive computations. Fortunately, for  $\text{LuCu}(\text{OH})_3\text{SO}_4$  with a small tilt angle

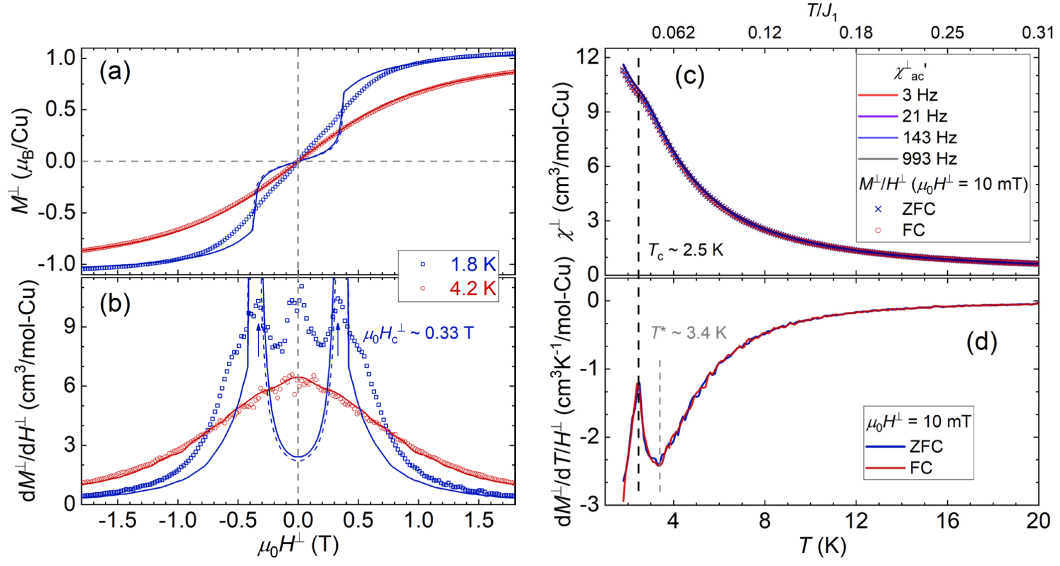


FIG. 4. Magnetization measured on the single-crystal sample. Isothermal (a) magnetization ( $M^\perp$ ) and (b) susceptibilities ( $dM^\perp/dH^\perp$ ) along the  $b$  axis. Solid and dashed colored lines represent SSE simulations with the self-consistent mean-field treatment of interchain interactions, using  $\delta = 3.8$  and  $-2.0$ , respectively; the solid and dashed red lines (at 4.2 K) overlap. The critical field of  $\mu_0 H_c^\perp \sim 0.33$  T is indicated by arrows in (b). Although complete loops were measured, no evident magnetic hysteresis was detected. (c) Ac susceptibilities measured at various frequencies, and dc susceptibilities measured under zero-field cooling (ZFC) and field cooling (FC). (d) The  $T$ -derivative magnetization at  $\mu_0 H^\perp = 10$  mT. The critical temperature  $T_c$  ( $\sim 2.5$  K) and the onset temperature  $T^*$  ( $\sim 3.4$  K) are indicated by dashed lines.

$\phi_0 = \arctan(D/J_1) \sim 6^\circ$ , the differences in observables using  $\tilde{\mathcal{H}}$  (Equation (3)) plus  $\tilde{\mathcal{H}}_Z^\perp$  (DM, exact) and  $\mathcal{H}_Z^\perp$  (XXZ, effective) are negligible within the temperature-field range of our experiments. For magnetization/susceptibility, we find  $1 < M_{\text{XXZ}}^\perp/M_{\text{DM}}^\perp \leq 1.003$  ( $\sim 1/\cos\phi_0$ ), which is nearly independent of the chain length  $N$  [38]. Similarly, the differences in calculated specific heat  $C_{\text{XXZ}}^\perp$  and  $C_{\text{DM}}^\perp$  are also completely negligible, compared to the experimental standard errors. Therefore, below, we utilize  $\tilde{\mathcal{H}}$  (Equation (3)) plus  $\mathcal{H}_Z^\parallel$  or  $\mathcal{H}_Z^\perp$  to simulate the magnetization and specific heat down to low temperatures, using the integrable Bethe ansatz method (only available for  $H \parallel z$  and  $N \rightarrow \infty$ ) [51–54] and 100-site ( $N = 100$ ) SSE quantum Monte Carlo algorithm [55, 56].

#### D. Perturbations beyond the nearest neighbors

Our semi-quantitative DFT+ $U$  simulations [38] suggest that the NNN intrachain coupling is weakly antiferromagnetic in  $\text{LuCu}(\text{OH})_3\text{SO}_4$ ,  $J_2/J_1 \sim 1\%$ . The antiferromagnetic  $J_2$  induces spin frustration and the notorious sign problem, generally impeding exact resolutions. Fortunately,  $J_2/J_1$  in  $\text{LuCu}(\text{OH})_3\text{SO}_4$  is significantly smaller,  $\sim 1\%$ , compared to the critical value  $J_2^c/J_1 = 25\%$  reported in the theoretical works [11, 12]. Furthermore, our many-body simulations confirm the negligible effects of the NNN intrachain coupling ( $J_2 = 1\%J_1$ ) on both magnetization and specific heat [38]. Hence, we can safely disregard the  $J_2$  terms in the effective XXZ Hamiltonian of Eq. (3).

Conversely, the minor interchain couplings can trigger a

magnetic transition and notably influence observations at low temperatures. Despite the strong ferromagnetic intrachain coupling, the presence of weak but non-negligible interchain couplings induces a three-dimensional (3D) antiferromagnetic order below  $T_c = 2.5$  K (see below), akin to observations in  $\text{Li}_2\text{CuO}_2$  [24] and  $\text{Ca}_2\text{Y}_2\text{Cu}_5\text{O}_{12}$  [27]. For simplicity, we address these small interchain couplings at a mean-field level for  $H^\perp > H_c^\perp$  [see Fig. 3(a)],

$$\begin{aligned} \tilde{\mathcal{H}}^\perp = & -\sqrt{J_1^2 + D^2} \sum_j (S_j^x S_{j+1}^x + S_j^y S_{j+1}^y + \Delta S_j^z S_{j+1}^z) \\ & - (\mu_0 H^\perp g^\perp - 6J_p \langle S^x \rangle) \sum_j S_j^x, \quad (4) \end{aligned}$$

where  $J_p = J_{1p}/3 + 2J_{2p}/3$ . After a sufficient number of self-consistent iterations ( $\geq 200$ ), we obtain the transverse magnetization  $M_{\text{calc}}^\perp = g^\perp \langle S^x \rangle = g^\perp \langle \sum_j S_j^x \rangle / N$ , which is independent of the iteration number. Combined fits to the transverse magnetization ( $M^\perp/H^\perp$ ) measured at  $\mu_0 H^\perp = 1$  and 3 T result in the least standard deviation  $\sigma = \sqrt{\sum_j (M_{\text{expt},j}^\perp/H_j^\perp - M_{\text{calc},j}^\perp/H_j^\perp)^2 / N_d} = 0.0358$   $\text{cm}^3/\text{mol-Cu}$  at  $J_p/J_1 = 0.21\%$  [see Fig. 2(d)]. Here,  $N_d$  represents the number of experimental data points.

Treating  $J_{p1}$  and  $J_{p2}$  at the mean-field level reveals two interchain antiferromagnetic orders at low temperatures and magnetic fields: stripe-I order at  $J_{p1} > J_{p2}$  and stripe-II order at  $J_{p1} < J_{p2}$  (see Fig. 3). Fitting to the critical magnetic field measured at 1.8 K,  $\mu_0 H_c^\perp = 0.33(2)$  T, yields two optimal sets of interchain couplings at  $J_p/J_1 = 0.21\%$ : I.  $J_{p1}/J_1 = 1.01\%$  and  $J_{p2}/J_1 = -0.18\%$ . II.  $J_{p1}/J_1 = -0.21\%$  and

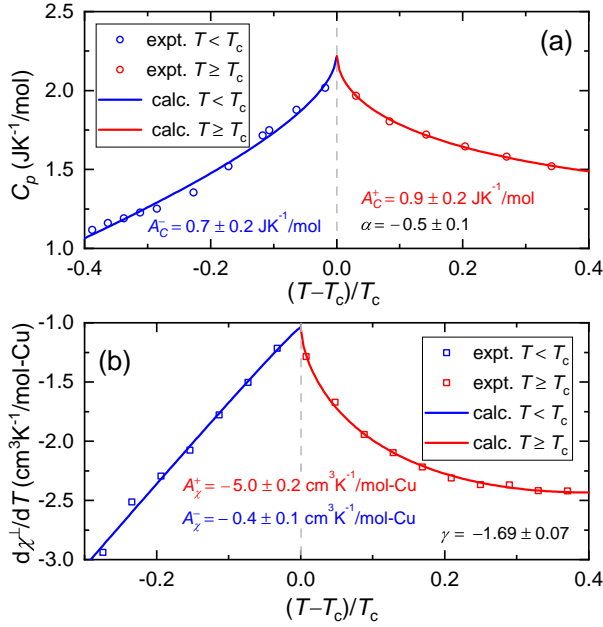


FIG. 5. Temperature dependence of (a) zero-field specific heat ( $C_p$ ) and (b)  $T$ -derivative dc susceptibility ( $d\chi^\pm/dT = dM^\pm/dT/H^\perp$ , where  $\mu_0 H^\perp = 0.01$  T is applied along the  $b$  axis) measured on  $\text{LuCu}(\text{OH})_3\text{SO}_4$ . The specific heat data is fitted to  $C_p = \frac{A_C^\pm}{\alpha} |t|^{-\alpha} + B_C + E_C t$  whereas the dc susceptibility data is fitted to  $d\chi^\pm/dT = \mp \gamma A_\chi^\pm |t|^{-\gamma-1} + B_\chi + E_\chi t$ , at  $T \geq T_c$  (+) and  $T < T_c$  (-), respectively. Here,  $A_C^\pm$  and  $A_\chi^\pm$  represent critical-behavior coefficients, the fitted critical exponents  $\alpha$  and  $\gamma$  are listed,  $B_C + E_C t$  and  $B_\chi + E_\chi t$  are caused by non-critical components in a linear- $t$  approximation,  $t \equiv (T - T_c)/T_c$ , and  $T_c = 2.5$  K.

$J_{p2}/J_1 = 0.42\%$  [Fig. 3(a)]. Both parameter sets agree with the critical temperature  $T_c$  measured at  $\sim 0$  T [see Figs. 3(b) and 3(c)] and well reproduce the magnetization/susceptibility measured on the single-crystal sample at 4.2 K [see Figs. 4(a) and 4(b)]. While we cannot presently distinguish which set of interchain couplings is more applicable for  $\text{LuCu}(\text{OH})_3\text{SO}_4$  based solely on the experimental data, the DFT+ $U$  calculations suggest the dominant antiferromagnetic nature of  $J_{p1}$ , favoring the parameter set I and thus the stripe-I interchain magnetic order.

Our self-consistent mean-field SSE method accurately simulates the experimental data at  $T \geq 4.2$  K ( $> T_c$ ) or  $\mu_0 H^\perp \geq 1$  T ( $> \mu_0 H_c^\perp$ ), where the symmetry of the spin system is fully recovered by thermal fluctuations or Zeeman interaction [see Figs. 2(d), 3, 4(a), and 4(b)]. Moreover, the mean-field model also shows excellent agreement with the boundary of  $\mu_0 H_c^\perp(T)$  and  $T_c(H^\perp)$  in the  $B$ - $T$  phase measured on  $\text{LuCu}(\text{OH})_3\text{SO}_4$  [38]. Nevertheless, the calculated magnetic-field-induced transition is considerably sharper than the experimental observations at 1.8 K [see Fig. 4(b)]. Additionally, the mean-field calculations fall short in accurately reproducing the experimental data at low temperatures and magnetic fields (within or near the interchain ordered phase). These discrepancies may stem from neglecting intrachain quantum

spin fluctuations in the mean-field treatment of interchain couplings.

In  $\text{LuCu}(\text{OH})_3\text{SO}_4$ , the putative interchain antiferromagnetic transition is likely significantly suppressed by the strong quantum spin fluctuations along the chain, as indicated by the weak kinks in susceptibility [ $dM^\pm/dH^\perp$ , Fig. 4(b)], magnetization [Figs. 4(c) and 4(d)], and specific heat [Fig. 5(a)] at critical points. The observed peaks in  $dM^\pm/dH^\perp$  and  $dM^\pm/dT/H^\perp$  [Figs. 4(b) and 4(d)] suggest that these temperature- and field-induced magnetic transitions are of second-order. The absence of frequency dependence in ac susceptibilities, the lack of splitting between ZFC and FC dc susceptibilities [Fig. 4(c)], and the absence of evident magnetic hysteresis in magnetization [Fig. 4(a)] exclude the possibilities of glassy or ferromagnetic nature for these transitions. Finally, as shown in the  $B$ - $T$  phase diagram [38], a weak applied field above  $\sim 0.6$  T, corresponding to an energy of  $\mu_0 H g \mu_B \sim 1\% J_1$ , is large enough to overcome the interchain antiferromagnetic correlations driven by  $J_{p1}/J_1 = 1.01\%$  and  $J_{p2}/J_1 = -0.18\%$  (as discussed above).

Following Refs. [57–59], we conducted traditional Kornblit-Ahlers-Buehler fits to the experimental thermodynamic properties of  $\text{LuCu}(\text{OH})_3\text{SO}_4$  near  $T_c = 2.5$  K, as depicted in Fig. 5. However, the fitted critical exponents,  $\alpha \sim -0.5$  and  $\gamma \sim -1.7$ , are significantly smaller than the theoretically predicted values for 3D systems [59]. This discrepancy suggests much broader peaks observed in both  $C_p$  and  $d\chi/dT$  (or  $\chi$ ) of  $\text{LuCu}(\text{OH})_3\text{SO}_4$  at  $T_c = 2.5$  K, indicating very unconventional critical behaviors, likely influenced by strong intrachain spin fluctuations. We emphasize that the negative sign of  $\gamma$  is a special novel feature of  $\text{LuCu}(\text{OH})_3\text{SO}_4$ , compared to other compounds [59]. This is confirmed by the measured raw susceptibilities, which are (nearly) monotonic functions of temperature, and exhibit only a weak kink at  $T_c = 2.5$  K (similar to the specific heat, see Fig. 6(a)), as shown in Fig. 4(c). The measured values of both  $\alpha$  and  $\gamma$  can determine the type of the phase transition, which may be useful in future theoretical and experimental investigations.

The weak but nonzero interchain antiferromagnetic couplings could induce a 3D Néel order (see Fig. 3).  $\text{LuCu}(\text{OH})_3\text{SO}_4$  only approximates the pure XXZ-chain model, and nonzero interchain couplings are inevitable. As illustrated in Fig. 4(d),  $T^* \sim 3.4$  K denotes the higher temperature at which the  $T$ -derivative magnetization/susceptibility  $dM/dT/H$  exhibits anomalies. It approaches the critical temperature  $T_c = 2.5$  K, prompting us to define it as the onset temperature of the proposed 3D Néel magnetic order (see Fig. 3).

## E. Proximate Tomonaga-Luttinger liquid state

The above observations and simulations suggest that the perturbation interactions beyond the nearest neighbors are weak and only have a marginal effect on the quantum magnetism of  $\text{LuCu}(\text{OH})_3\text{SO}_4$ . Since these perturbations are inherent and completely unavoidable in any real materials, we propose  $\text{LuCu}(\text{OH})_3\text{SO}_4$  as the most perfect candidate so far for the ideal spin-1/2 ferromagnetic XXZ chain model

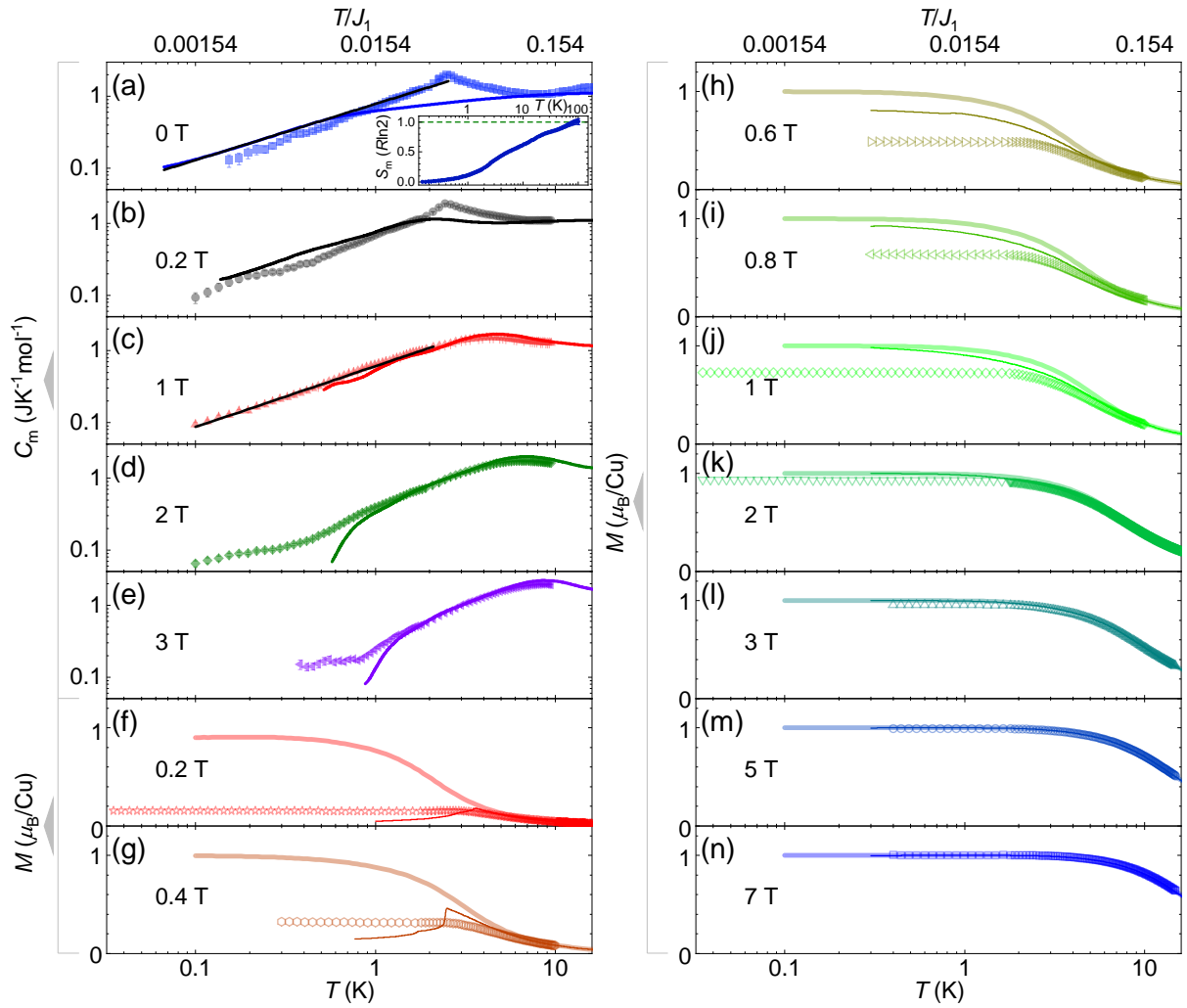


FIG. 6. (a)-(e) Low- $T$  magnetic specific heat ( $C_m$ ) measured on  $\text{LuCu}(\text{OH})_3\text{SO}_4$  powder. The lattice contribution is carefully evaluated and subtracted from the total measured specific heat [38]. The zero-field specific heat is calculated using the Bethe ansatz method [blue line, see (a)], while the nonzero-field data are computed by the SSE method [colored lines, see (b)-(e)]. Here,  $J_1 = 65$  K and  $\Delta = 0.994$  (ideal XXZ-chain model) are used, and the nonzero-field calculations are powder-averaged,  $C_{m,\text{calc}} = 2C_{m,\text{SSE}}^\perp/3 + C_{m,\text{Bethe}}^\parallel/3$  [38]. The black line shows a power-law fit to the experimental data measured at 1 T (red triangles) below 2 K in (c),  $C_m \propto T^{0.848(7)}$ , whereas the black line in (a) displays a power-law fit to the zero-field calculated (Bethe) data between 0.1 and 0.6 K,  $C_{m,\text{Bethe}}(0 \text{ T}) \propto T^{0.782(2)}$ . The inset of (a) displays the zero-field magnetic entropy integrated from the experimental data,  $S_m(T) = \int_{0.15\text{K}}^T C_m(T')dT'/T'$ . (f)-(n) Low- $T$  magnetization measured on  $\text{LuCu}(\text{OH})_3\text{SO}_4$  powder. The thick and thin lines respectively present SSE calculations using the ideal XXZ-chain model ( $J_1 = 65$  K and  $\Delta = 0.994$ ) and detailed model (with additional  $J_{p1}/J_1 = 1.01\%$  and  $J_{p2}/J_1 = -0.18\%$ ) in a powder average. In the detailed model, interchain interactions are treated by a self-consistent mean-field approximation.

[see Eq. (3) with  $\mathcal{H}' \sim 0$ ]. Therefore, below we focus on the direct comparisons between the low- $T$  observations and theoretical expectations of the ideal exactly solvable model (Fig. 6). When the chain length  $N$  is less than  $\sim 30$ , the ED/SSE simulations exhibit evident finite-size effects below  $\sim 8$  K ( $\sim 0.1J_1$ ) despite the periodic boundary condition employed [38], suggesting highly exotic ground-state properties of the spin-1/2 ferromagnetic XXZ chain system with long-distance unconventional entanglements.

It remains technically difficult to measure the single-crystal specific heat and mK magnetization, limited by the crystal

size [38]. In the following discussions, we rely on the low- $T$  data measured on the ground powder.  $\text{LuCu}(\text{OH})_3\text{SO}_4$  is suggested to approximate a gapless Tomonaga-Luttinger liquid ground state of the ideal spin-1/2 ferromagnetic XXZ chain model, supported by: 1. Both our experimental data (Figs. 2 and 3) and DFT+ $U$  calculations consistently demonstrate  $\Delta \sim 0.994$  and  $J_2/J_1 \sim 1\%$  ( $\ll 1/4$ ), suggesting  $\text{LuCu}(\text{OH})_3\text{SO}_4$  is deeply inside the Tomonaga-Luttinger-liquid-ground-state region [11, 12]. 2. The magnetic entropy measured at 0 T approaches zero at low temperatures ( $< 2$  K) from the full value of  $R\ln(1+2S) = R\ln 2$  at high temperatures ( $\sim 100$  K),

where  $S = 1/2$  [see inset of Fig. 6(a)]. This indicates the spin-1/2 ( $\text{Cu}^{2+}$ ) system of  $\text{LuCu}(\text{OH})_3\text{SO}_4$  indeed approaches its ground-state properties below  $\sim 2$  K ( $\sim 3\%J_1$ ). 3. Below  $\sim 2$  K, the magnetic specific heat exhibits a power-law temperature dependence down to the lowest measured temperature [ $\sim 0.1$  K, see Fig. 6(c)],  $C_m \propto T^{0.85}$ , at low applied fields of  $\leq 1$  T ( $\mu_0 H g \mu_B \leq 2\%J_1$ ). Moreover, the dc magnetization measured at  $\mu_0 H = 0.2$  T flattens out to an unsaturated value ( $< g/2$ ) below  $\sim 2$  K. These observations strongly suggest the gapless nature of the low-lying spin excitations in  $\text{LuCu}(\text{OH})_3\text{SO}_4$ . 4. The ideal spin-1/2 ferromagnetic XXZ chain model ( $J_1 = 65$  K and  $\Delta = 0.994$ ) yields the exactly solved specific heat between  $\sim 0.1$  and  $0.6$  K,  $C_{m,\text{Bethe}}(0 \text{ T}) \propto T^{0.782(2)}$  [Fig. 6(a)], in good agreement with the experimental findings. The calculated magnetization at  $0.2$  T also flattens out at low temperatures, qualitatively consistent with the experimental result [Fig. 6(f)].

The applied magnetic field can shift the nuclear Schottky specific heat to higher temperatures [41], possibly contributing to the larger distinctions between the experimental and calculated data at low temperatures in  $2$  and  $3$  T [Figs. 6(d) and 6(e)]. Interchain interactions have a minor effect on specific heat, except for the weak peak centered at  $T_c \sim 2.5$  K observed at  $\mu_0 H < 1$  T. In contrast, interchain interactions ( $J_{p1}$  and  $J_{p2}$ ) significantly suppress magnetization at low temperatures and low applied fields, providing a better explanation for the experimental findings [Figs. 6(f)-6(n)]. Since interchain interactions are treated only at the mean-field level, and a powder average is adopted to lower the computational cost, achieving full quantitative agreement between experimental and simulated magnetization data at low temperatures and ap-

plied fields remains extremely challenging. Improved treatment of interchain interactions and larger-size single crystals of  $\text{LuCu}(\text{OH})_3\text{SO}_4$  are highly required for further studies.

#### IV. CONCLUSIONS

We propose  $\text{LuCu}(\text{OH})_3\text{SO}_4$ , a structurally disorder-free compound, as a promising candidate for the exactly solvable spin-1/2 ferromagnetic XXZ chain model ( $J_1 = 65$  K and  $\Delta = 0.994$ ). Determined small values for the interchain and NNN intrachain interactions ( $J_{p1}/J_1 \sim 1.01\%$ , and  $J_{p2}/J_1 \sim -0.18\%$ , and  $J_2/J_1 \sim 1\%$ ) support this candidacy. Measurements of specific heat and magnetization down to  $T = 35$  mK ( $\sim 0.0005J_1$ ) exhibit gapless ground-state behaviors, aligning with theoretical expectations for the ideal model. These observations indicate that  $\text{LuCu}(\text{OH})_3\text{SO}_4$  approximates a gapless Tomonaga-Luttinger liquid state at low temperatures. Our findings mark an initial step towards understanding the potential Tomonaga-Luttinger liquid phase in  $\text{LuCu}(\text{OH})_3\text{SO}_4$  and offer new insights for experimental investigations into exactly solvable strongly correlated quantum systems.

#### ACKNOWLEDGMENTS

We gratefully acknowledge Haijun Liao for helpful discussion. This work was supported by the National Key R&D Program of China (Grant No. 2023YFA1406500), the National Natural Science Foundation of China (No. 12274153), and the Fundamental Research Funds for the Central Universities (No. HUST: 2020kfyXJJS054).

- 
- [1] C. Nayak, S. H. Simon, A. Stern, M. Freedman, and S. Das Sarma, “Non-Abelian anyons and topological quantum computation,” *Rev. Mod. Phys.* **80**, 1083 (2008).
- [2] S. Yan, D. A. Huse, and S. R. White, “Spin-liquid ground state of the  $S = 1/2$  kagome Heisenberg antiferromagnet,” *Science* **332**, 1173–1176 (2011).
- [3] S. Depenbrock, I. P. McCulloch, and U. Schollwöck, “Nature of the spin-liquid ground state of the  $S = 1/2$  Heisenberg model on the kagome lattice,” *Phys. Rev. Lett.* **109**, 067201 (2012).
- [4] Y. Ran, M. Hermele, P. A. Lee, and X.-G. Wen, “Projected-wave-function study of the spin-1/2 Heisenberg model on the kagomé lattice,” *Phys. Rev. Lett.* **98**, 117205 (2007).
- [5] H. J. Liao, Z. Y. Xie, J. Chen, Z. Y. Liu, H. D. Xie, R. Z. Huang, B. Normand, and T. Xiang, “Gapless spin-liquid ground state in the  $S = 1/2$  kagome antiferromagnet,” *Phys. Rev. Lett.* **118**, 137202 (2017).
- [6] A. Kitaev, “Anyons in an exactly solved model and beyond,” *Ann. Phys.* **321**, 2–111 (2006).
- [7] L. Janssen, E. C. Andrade, and M. Vojta, “Magnetization processes of zigzag states on the honeycomb lattice: Identifying spin models for  $\alpha\text{-RuCl}_3$  and  $\text{Na}_2\text{IrO}_3$ ,” *Phys. Rev. B* **96**, 064430 (2017).
- [8] J. Wang, B. Normand, and Z.-X. Liu, “One proximate Kitaev spin liquid in the K-J- $\Gamma$  model on the honeycomb lattice,” *Phys. Rev. Lett.* **123**, 197201 (2019).
- [9] H. Bethe, “Zur Theorie der Metalle. I. Eigenwerte und Eigenfunktionen der linearen Atomkette,” *Z. Phys.* **71**, 205–226 (1931).
- [10] W. Heisenberg, *Zur Theorie des Ferromagnetismus*, Vol. 49 (Springer, 1985) pp. 619–636.
- [11] S. Furukawa, M. Sato, and A. Furusaki, “Unconventional Néel and dimer orders in a spin- $\frac{1}{2}$  frustrated ferromagnetic chain with easy-plane anisotropy,” *Phys. Rev. B* **81**, 094430 (2010).
- [12] S. Furukawa, M. Sato, S. Onoda, and A. Furusaki, “Ground-state phase diagram of a spin- $\frac{1}{2}$  frustrated ferromagnetic XXZ chain: Haldane dimer phase and gapped/gapless chiral phases,” *Phys. Rev. B* **86**, 094417 (2012).
- [13] M. Enderle, B. Fåk, H.-J. Mikeska, R. K. Kremer, A. Prokofiev, and W. Assmus, “Two-spinon and four-spinon continuum in a frustrated ferromagnetic spin-1/2 chain,” *Phys. Rev. Lett.* **104**, 237207 (2010).
- [14] S.-L. Drechsler, S. Nishimoto, R. O. Kuzian, J. Málek, W. E. A. Lorenz, J. Richter, J. van den Brink, M. Schmitt, and H. Rosner, “Comment on ‘Two-spinon and four-spinon continuum in a frustrated ferromagnetic spin-1/2 chain’,” *Phys. Rev. Lett.* **106**, 219701 (2011).
- [15] M. Mourigal, M. Enderle, B. Fåk, R. K. Kremer, J. M. Law, A. Schneidewind, A. Hiess, and A. Prokofiev, “Evidence of a

- bond-nematic phase in  $\text{LiCuVO}_4$ ,” *Phys. Rev. Lett.* **109**, 027203 (2012).
- [16] K. Nawa, M. Takigawa, M. Yoshida, and K. Yoshimura, “Anisotropic spin fluctuations in the quasi one-dimensional frustrated magnet  $\text{LiCuVO}_4$ ,” *J. Phys. Soc. Jpn.* **82**, 094709 (2013).
- [17] A. Ruff, P. Lunkenheimer, H. K. von Nidda, S. Widmann, A. Prokofiev, L. Svistov, A. Loidl, and S. Krohns, “Chirality-driven ferroelectricity in  $\text{LiCuVO}_4$ ,” *npj Quant. Mater.* **4**, 24 (2019).
- [18] S. E. Dutton, M. Kumar, M. Mourigal, Z. G. Soos, J.-J. Wen, C. L. Broholm, N. H. Andersen, Q. Huang, M. Zbiri, R. Toft-Petersen, and R. J. Cava, “Quantum spin liquid in frustrated one-dimensional  $\text{LiCuSbO}_4$ ,” *Phys. Rev. Lett.* **108**, 187206 (2012).
- [19] H.-J. Grafe, S. Nishimoto, M. Iakovleva, E. Vavilova, L. Spillecke, A. Alfonsov, M.-I. Sturza, S. Wurmehl, H. Nojiri, H. Rosner, J. Richter, U. K. Rößler, S.-L. Drechsler, V. Kataev, and B. Büchner, “Signatures of a magnetic field-induced unconventional nematic liquid in the frustrated and anisotropic spin-chain cuprate  $\text{LiCuSbO}_4$ ,” *Sci. Rep.* **7**, 6720 (2017).
- [20] M. Bosiočić, F. Bert, S. E. Dutton, R. J. Cava, P. J. Baker, M. Požek, and P. Mendels, “Possible quadrupolar nematic phase in the frustrated spin chain  $\text{LiCuSbO}_4$ : An NMR investigation,” *Phys. Rev. B* **96**, 224424 (2017).
- [21] C. Dussarrat, G. C. Mather, V. Caignaert, B. Domengès, J. G. Fletcher, and A. R. West, “Synthesis and crystal structures of  $\text{Li}_2\text{CuZrO}_4$  polymorphs,” *J. Solid State Chem.* **166**, 311–319 (2002).
- [22] S.-L. Drechsler, O. Volkova, A. N. Vasiliev, N. Tristan, J. Richter, M. Schmitt, H. Rosner, J. Málek, R. Klingeler, A. A. Zvyagin, and B. Büchner, “Frustrated cuprate route from antiferromagnetic to ferromagnetic spin- $\frac{1}{2}$  Heisenberg chains:  $\text{Li}_2\text{CuZrO}_4$  as a missing link near the quantum critical point,” *Phys. Rev. Lett.* **98**, 077202 (2007).
- [23] F. Sapina, J. Rodriguez-Carvajal, M.J. Sanchis, R. Ibanez, A. Beltran, and D. Beltran, “Crystal and magnetic structure of  $\text{Li}_2\text{CuO}_2$ ,” *Solid State Commun.* **74**, 779–784 (1990).
- [24] W.E.A. Lorenz, R.O. Kuzian, S.-L. Drechsler, W.-D. Stein, N. Wizen, G. Behr, J. Málek, U. Nitzsche, H. Rosner, A. Hiess, W. Schmidt, R. Klingeler, M. Loewenhaupt, and B. Büchner, “Highly dispersive spin excitations in the chain cuprate  $\text{Li}_2\text{CuO}_2$ ,” *Europhys. Lett.* **88**, 37002 (2009).
- [25] R. O. Kuzian, S. Nishimoto, S.-L. Drechsler, J. Málek, S. Johnston, Jeroen van den Brink, M. Schmitt, H. Rosner, M. Matsuda, K. Oka, H. Yamaguchi, and T. Ito, “ $\text{Ca}_2\text{Y}_2\text{Cu}_5\text{O}_{10}$ : The first frustrated quasi-1D ferromagnet close to criticality,” *Phys. Rev. Lett.* **109**, 117207 (2012).
- [26] J. Thar, R. Müller, S. Mattauch, B. Büchner, and G. A. Roth, “Neutron structure investigation of  $\text{Ca}_2\text{Y}_2\text{Cu}_5\text{O}_{10}$ ,” *Acta Cryst. A* **62**, 185–185 (2006).
- [27] M. Matsuda, J. Ma, V. O. Garlea, T. Ito, H. Yamaguchi, K. Oka, S.-L. Drechsler, R. Yadav, L. Hozoi, H. Rosner, R. Schumann, R. O. Kuzian, and S. Nishimoto, “Highly dispersive magnons with spin-gap-like features in the frustrated ferromagnetic  $S = \frac{1}{2}$  chain compound  $\text{Ca}_2\text{Y}_2\text{Cu}_5\text{O}_{10}$  detected by inelastic neutron scattering,” *Phys. Rev. B* **100**, 104415 (2019).
- [28] K. Caslin, R. K. Kremer, F. S. Razavi, A. Schulz, A. Muñoz, F. Pertlik, J. Liu, M.-H. Whangbo, and J. M. Law, “Characterization of the spin- $\frac{1}{2}$  linear-chain ferromagnet  $\text{CuAs}_2\text{O}_4$ ,” *Phys. Rev. B* **89**, 014412 (2014).
- [29] B. Willenberg, M. Schäpers, K. C. Rule, S. Stillow, M. Reehuis, H. Ryll, B. Klemke, K. Kiefer, W. Schottenhamel, B. Büchner, B. Ouladdiaf, M. Uhlarz, R. Beyer, J. Wosnitsa, and A. U. B. Wolter, “Magnetic frustration in a quantum spin chain: The case of linarite  $\text{PbCuSO}_4(\text{OH})_2$ ,” *Phys. Rev. Lett.* **108**, 117202 (2012).
- [30] L. Heinze, M. D. Le, O. Janson, S. Nishimoto, A. U. B. Wolter, S. Stillow, and K. C. Rule, “Low-energy spin excitations of the frustrated ferromagnetic  $J_1$ - $J_2$  chain material linarite  $\text{PbCuSO}_4(\text{OH})_2$  in applied magnetic fields parallel to the  $b$  axis,” *Phys. Rev. B* **106**, 144409 (2022).
- [31] W. Wang, Y. Qiao, J. P. Cao, W. M. Liu, and R. H. Liu, “Exact ground state and elementary excitations of a competing spin chain with twisted boundary condition,” *Nucl. Phys. B* **975**, 115663 (2022).
- [32] Y. Li, D. Adroja, R. I. Bewley, D. Voneshen, A. A. Tsirlin, P. Gegenwart, and Q. Zhang, “Crystalline electric-field randomness in the triangular lattice spin-liquid  $\text{YbMgGaO}_4$ ,” *Phys. Rev. Lett.* **118**, 107202 (2017).
- [33] Y. Li, “ $\text{YbMgGaO}_4$ : A triangular-lattice quantum spin liquid candidate,” *Adv. Quantum Technol.* **2**, 1900089 (2019).
- [34] Y. Li, S. Bachus, H. Deng, W. Schmidt, H. Thoma, V. Hutano, Y. Tokiwa, A. A. Tsirlin, and P. Gegenwart, “Partial up-up-down order with the continuously distributed order parameter in the triangular antiferromagnet  $\text{TmMgGaO}_4$ ,” *Phys. Rev. X* **10**, 011007 (2020).
- [35] Y. Li, Q.-Y. Li, W. Li, T. Liu, D. J. Voneshen, P. K. Biswas, and D. Adroja, “Spin dynamics and Griffiths singularity in the random quantum Ising magnet  $\text{PrTiNbO}_6$ ,” *npj Quantum Mater.* **6**, 34 (2021).
- [36] F. Lu, L. Yuan, J. Zhang, B. Li, Y. Luo, and Y. Li, “The observation of quantum fluctuations in a kagome Heisenberg antiferromagnet,” *Commun. Phys.* **5**, 272 (2022).
- [37] H. J. Lu, K. Diefenbach, Z.-J. Li, H. L. Bao, X. F. Guo, J.-Q. Wang, T. E. Albrecht-Schmitt, and J. Lin, “Structural complexity and magnetic orderings in a large family of 3d-4f heterobimetallic sulfates,” *Inorg. Chem.* **59**, 13398–13406 (2020).
- [38] *See Supplementary Material for detailed information about experimental and numerical procedures, which includes Refs. [60–64].*
- [39] Y. Shimizu, Y. Kono, T. Sugiyama, S. Kittaka, Y. Shimura, A. Miyake, D. Aoki, and T. Sakakibara, “Development of high-resolution capacitive Faraday magnetometers for sub-Kelvin region,” *Rev. Sci. Instrum.* **92**, 123908 (2021).
- [40] Y. Li, S. Bachus, B. Liu, I. Radelytskyi, A. Bertin, A. Schneidewind, Y. Tokiwa, A. A. Tsirlin, and P. Gegenwart, “Rearrangement of uncorrelated valence bonds evidenced by low-energy spin excitations in  $\text{YbMgGaO}_4$ ,” *Phys. Rev. Lett.* **122**, 137201 (2019).
- [41] Y. Li, S. Bachus, Y. Tokiwa, A. A. Tsirlin, and P. Gegenwart, “Gapped ground state in the zigzag pseudospin-1/2 quantum antiferromagnetic chain compound  $\text{PrTiNbO}_6$ ,” *Phys. Rev. B* **97**, 184434 (2018).
- [42] J. Liu, L. Yuan, X. Li, B. Li, K. Zhao, H. Liao, and Y. Li, “Gapless spin liquid behavior in a kagome Heisenberg antiferromagnet with randomly distributed hexagons of alternate bonds,” *Phys. Rev. B* **105**, 024418 (2022).
- [43] T. Moriya, “Anisotropic superexchange interaction and weak ferromagnetism,” *Phys. Rev.* **120**, 91–98 (1960).
- [44] A. Zorko, S. Nellutla, J. van Tol, L. C. Brunel, F. Bert, F. Duc, J.-C. Trombe, M. A. de Vries, A. Harrison, and P. Mendels, “Dzyaloshinsky-Moriya anisotropy in the spin-1/2 kagome compound  $\text{ZnCu}_3(\text{OH})_6\text{Cl}_2$ ,” *Phys. Rev. Lett.* **101**, 026405 (2008).
- [45] In  $\text{LuCu}(\text{OH})_3\text{SO}_4$ , each unit cell contains two spins along each chain.

- [46] Y. Li, G. Chen, W. Tong, L. Pi, J. Liu, Z. Yang, X. Wang, and Q. Zhang, “Rare-earth triangular lattice spin liquid: A single-crystal study of  $\text{YbMgGaO}_4$ ,” *Phys. Rev. Lett.* **115**, 167203 (2015).
- [47] A. C. Saladino and S. C. Larsen, “Relativistic dft calculations of copper hyperfine coupling constants: Effect of spin-orbit coupling,” *J. Phys. Chem. A* **107**, 5583–5587 (2003).
- [48] J. Liu, B. Liu, L. Yuan, B. Li, L. Xie, X. Chen, H. Zhang, D. Xu, W. Tong, J. Wang, and Y. Li, “Frustrated magnetism of the triangular-lattice antiferromagnets  $\alpha\text{-CrOOH}$  and  $\alpha\text{-CrOOD}$ ,” *New J. Phys.* **23**, 033040 (2021).
- [49] T. G. Castner and M. S. Seehra, “Antisymmetric exchange and exchange-narrowed electron-paramagnetic-resonance linewidths,” *Phys. Rev. B* **4**, 38–45 (1971).
- [50] D. N. Aristov and S. V. Maleyev, “Spin chirality induced by the Dzyaloshinskii-Moriya interaction and polarized neutron scattering,” *Phys. Rev. B* **62**, R751–R754 (2000).
- [51] M. Takahashi and M. Yamada, “Spin-1/2 one-dimensional Heisenberg ferromagnet at low-temperature,” *J. Phys. Soc. Jpn.* **54**, 2808–2811 (1985).
- [52] P. Schlottmann, “Critical behavior of the isotropic ferromagnetic quantum Heisenberg chain,” *Phys. Rev. Lett.* **54**, 2131–2134 (1985).
- [53] M. Takahashi, “Simplification of thermodynamic Bethe-Ansatz equations,” *World Sci.* , 299–304 (2001).
- [54] M. Takahashi, “Thermodynamics and correlation functions of XXZ chain,” *Czechoslov. J. Phys.* **53**, 1125–1130 (2003).
- [55] O. F. Syljuåsen and A. W. Sandvik, “Quantum Monte Carlo with directed loops,” *Phys. Rev. E* **66**, 046701 (2002).
- [56] A. W. Sandvik, “Stochastic series expansion method with operator-loop update,” *Phys. Rev. B* **59**, R14157–R14160 (1999).
- [57] A. Kornblit, G. Ahlers, and E. Buehler, “Heat capacity of  $\text{RbMnF}_3$  and  $\text{EuO}$  near the magnetic phase transitions,” *Phys. Lett. A* **43**, 531 (1973).
- [58] A. Kornblit and G. Ahlers, “Heat capacity of  $\text{EuO}$  near the Curie temperature,” *Phys. Rev. B* **11**, 2678–2688 (1975).
- [59] J. Wosnitza, “From thermodynamically driven phase transitions to quantum critical phenomena,” *J. Low Temp. Phys.* **147**, 249–278 (2007).
- [60] Y. Wang, S. Lany, J. Ghanbaja, Y. Fagot-Revurat, Y. P. Chen, F. Soldera, D. Horwat, F. Mücklich, and J. F. Pierson, “Electronic structures of  $\text{Cu}_2\text{O}$ ,  $\text{Cu}_4\text{O}_3$ , and  $\text{CuO}$ : A joint experimental and theoretical study,” *Phys. Rev. B* **94**, 245418 (2016).
- [61] G. Kresse and J. Furthmüller, “Efficiency of ab-initio total energy calculations for metals and semiconductors using a plane-wave basis set,” *Comp. Mater. Sci.* **6**, 15–50 (1996).
- [62] G. Kresse and J. Furthmüller, “Efficient iterative schemes for ab initio total-energy calculations using a plane-wave basis set,” *Phys. Rev. B* **54**, 11169–11186 (1996).
- [63] J. P. Perdew, K. Burke, and M. Ernzerhof, “Generalized gradient approximation made simple,” *Phys. Rev. Lett.* **77**, 3865–3868 (1996).
- [64] A. W. Sandvik, “Computational studies of quantum spin systems,” *AIP Conf. Proc.* **1297**, 135–338 (2010).

## *Supplementary material*

### **Proximate Tomonaga-Luttinger liquid in a spin-1/2 ferromagnetic XXZ chain compound**

Boqiang Li,<sup>1,\*</sup> Xun Chen,<sup>1,\*</sup> Yuqian Zhao,<sup>1,\*</sup> Zhaohua Ma,<sup>1</sup> Zongtang Wan,<sup>1</sup> and Yuesheng Li<sup>1,†</sup>

<sup>1</sup>*Wuhan National High Magnetic Field Center and School of Physics,  
Huazhong University of Science and Technology, 430074 Wuhan, China*

We present here:

#### **I. Sample synthesis and characterization.**

Fig. S1. Powder x-ray diffraction and Rietveld refinement analysis.

Fig. S2. Image of as-grown single crystals.

Fig. S3. Electron spin resonance spectrum measured on the powder sample.

Table S1. Crystal structure refined from powder x-ray diffraction data.

Table S2. Crystal structure refined from single-crystal x-ray diffraction data.

#### **II. Numerical methods and models.**

Table S3. Density functional theory calculations.

Fig. S4. Validation of the effective XXZ model and finite-size effects.

Fig. S5. Negligible effects of weak antiferromagnetic next-nearest-neighbor intrachain coupling and validation of the stochastic series expansion method.

Fig. S6. Extraction of lattice specific heat for  $\text{LuCu}(\text{OH})_3\text{SO}_4$ .

Fig. S7. Determinating the strength of the interchain coupling.

Fig. S8. Phase diagram of  $\text{LuCu}(\text{OH})_3\text{SO}_4$ .

---

\* These authors contributed equally to this work

† [yuesheng\\_li@hust.edu.cn](mailto:yuesheng_li@hust.edu.cn)

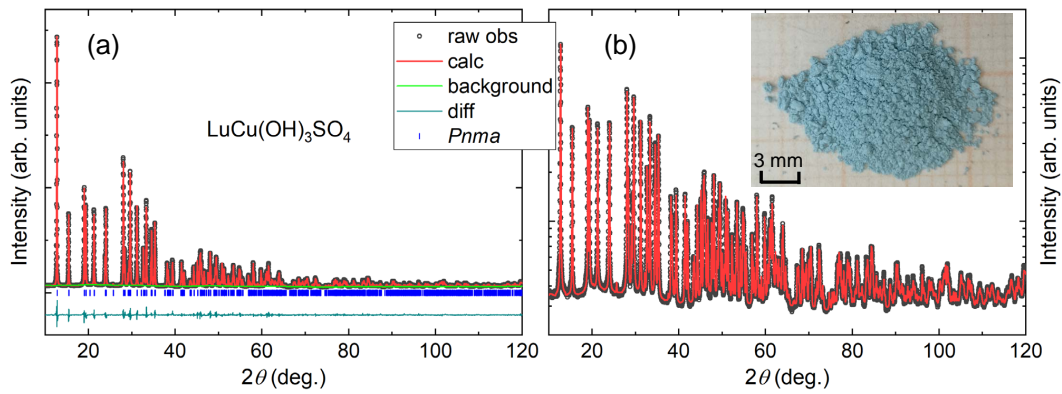


FIG. S1. (a) Powder x-ray diffraction and Rietveld refinement pattern for  $\text{LuCu}(\text{OH})_3\text{SO}_4$ . (b) A log10 intensity re-plot of the data. Inset: Powder sample ground from small crystals [see Fig. S2(a)].

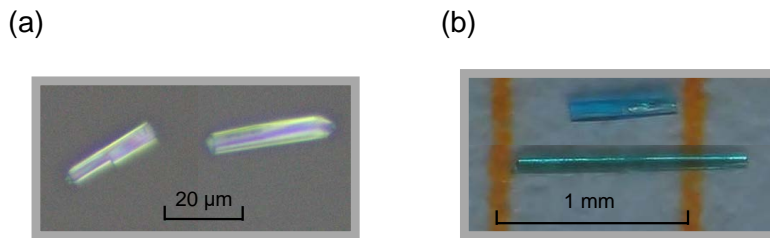
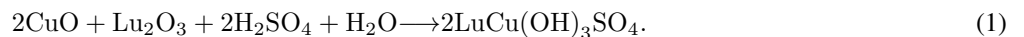


FIG. S2. Typical as-grown single crystals using a) CuO powders or b) copper plates as the Cu source in the synthesis processes. The  $b$  axis is along the longest dimension of each crystal. The slight color variations observed in samples may be attributed to differences in lighting and the microscopes used. The phase purities of  $\text{LuCu}(\text{OH})_3\text{SO}_4$  for both crystals shown in (b) have been confirmed through single-crystal XRD measurements. Both panels (a) and (b) are composed by stitching together two separate photographs, indicating that the images of the four crystals were captured under distinct lighting conditions. Furthermore, the photograph in (a) was acquired using a high-resolution optical microscope (Model: Zeiss Lattice SIM3) at a magnification of 1000 times, while (b) was captured using a standard microscope (Model: ZW-H3000) at a magnification of 50 times.

## I. SAMPLE SYNTHESIS AND CHARACTERIZATION

To synthesize  $\text{LuCu}(\text{OH})_3\text{SO}_4$ , we employed the traditional hydrothermal method, following the procedure reported in Ref. [1], and utilized CuO powder as the source of Cu,



$\text{Lu}_2\text{O}_3$  ( $\geq 99.99\%$ , Adamas Reagent Co., Ltd, 1 mmol, 0.398 g), CuO ( $\geq 99\%$ , Adamas Reagent Co., Ltd, 2 mmol, 0.159 g), 1 M  $\text{H}_2\text{SO}_4$  (2 mmol, 2 mL), and 2 mL high-purity  $\text{H}_2\text{O}$  were mixed and charged into a 100 ml Teflon-lined autoclave. The sealed autoclave was heated to 503 K and maintained for 3 days. Light blue crystals were obtained after rinsing, filtration, and drying. The powder ground from the crystals was analyzed by x-ray diffraction (XRD), revealing no impurity phase (see Fig. S1). The refined crystal structure (Table S1) aligns well with the previously reported results [1]. The typical size of these crystals, measured by a microscope, is  $5 \times 30 \times 5 \mu\text{m}$  [see Fig. S2(a)], consistent with the previously reported work [1]. The electron spin resonance (ESR) spectrum measured on the powder indicates only about 0.45% quasi-free magnetic moments (Fig. S3). However, these crystals are too small for alignment, and larger-size single crystals are essential to collecting anisotropic magnetic data for  $\text{LuCu}(\text{OH})_3\text{SO}_4$ .

A log10 intensity re-plot of the powder XRD data is presented in Fig. S1(b). In Fig. S1(a), we also display the background (green line), which remains nearly constant. The powder sample utilized in this XRD measurement is ground from as-grown small crystals to prevent orientation preference. Each crystal encompasses  $\sim 4000 \times 50000 \times 8000 \times 4 \sim 6 \times 10^{12}$  spins ( $\gg 30^3 = 2700$  spins, see below), and therefore, any finite-size effects of crystals on magnetic properties should be negligible. The sizes of

TABLE S1. The crystal structure of  $\text{LuCu}(\text{OH})_3\text{SO}_4$  refined from the powder XRD data (Fig. S1). Please note that the positions and thermal parameters of H atoms weren't refined and were kept the same as in Ref. [1], as XRD is insensitive to H atoms. The occupancy fractions were set to "1" for all atoms, following the methodology in Ref. [1].

space group	$Pnma$
$a$	13.87629(7) Å
$b$	6.07789(4) Å
$c$	6.29356(3) Å
Cell volume, $Z = 1$	530.791(4) Å <sup>3</sup>
Lu: $x, y, z$	0.41957(4), 0.25, 0.06358(8)
$U_{\text{iso}}$	0.0063(1)
Cu: $x, y, z$	0.5, 0, 0.5
$U_{\text{iso}}$	0.0020(4)
S: $x, y, z$	0.3086(2), 0.75, 0.2704(4)
$U_{\text{iso}}$	0.0122(8)
O1: $x, y, z$	0.4152(3), 0.25, 0.4444(7)
$U_{\text{iso}}$	0.0004±0.0014
O2: $x, y, z$	0.4612(3), 0.9949(6), 0.7977(4)
$U_{\text{iso}}$	0.022(2)
O3: $x, y, z$	0.2022(4), 0.75, 0.2974(7)
$U_{\text{iso}}$	0.013(2)
O4: $x, y, z$	0.3669(3), 0.75, 0.4676(8)
$U_{\text{iso}}$	0.0004±0.0016
O5: $x, y, z$	0.3251(3), 0.9402(6), 0.1414(5)
$U_{\text{iso}}$	0.020(2)
H1: $x, y, z$	0.3680, 0.2500, 0.5000
$U_{\text{iso}}$	0.024
H2: $x, y, z$	0.4210, 0.9480, 0.7930
$U_{\text{iso}}$	0.024
$R_p$	3.26%
$R_{wp}$	4.50%
$\chi^2$	10.31

small crystals were analyzed using a high-resolution optical microscope [see Fig. S2(a)], and no scanning electron microscope (SEM) was employed. Additionally,  $\text{LuCu}(\text{OH})_3\text{SO}_4$  is a good insulator, rendering SEM measurements potentially unsuitable.

The powder x-ray diffraction exhibits sharp Bragg reflections (see Fig. S1), with a full width at half maximum of  $2\Delta\theta = 0.100^\circ$  at the strongest reflection  $2\theta = 12.71^\circ$ . By accounting for the instrument resolution of  $0.05^\circ$ , the intrinsic broadening  $2\Delta\theta_0$  is determined to be  $0.074^\circ$ . Using the Scherrer equation, the particle size of the ground powder ( $P$ ) is estimated as  $P \geq \frac{K\lambda}{2\Delta\theta_0 \cos\theta} \sim 110$  nm, accounting for potential strain broadening. Here,  $K = 0.9$  is the Scherrer constant, and  $\lambda = 0.154184$  nm is the x-ray wavelength. Each particle in the powder sample contains on average  $\sim \frac{2\pi P^3}{3V_0} \geq 5.3 \times 10^6$  spins ( $\gg 30^3 = 2700$  spins, see below), where  $V_0 = 0.53$  nm<sup>3</sup> is the cell volume (see Table S1), and each unit cell contains 4 spins.

To increase crystal size, we reduced the chemical reaction rate by using pure copper (Cu  $\geq 99.99\%$ ) plates as the Cu source,



The corrosion process of copper plates by  $\text{H}_2\text{SO}_4$  is expected to be very slow, potentially allowing more time for crystal growth. The synthesis temperature of 503 K was maintained for 5 days and then cooled to room temperature at a rate of 8 K/hour. The typical size was increased to  $0.08 \times 1 \times 0.08$  mm, as shown in Fig. S2(b). Single-crystal XRD confirmed the  $\text{LuCu}(\text{OH})_3\text{SO}_4$  phase (Table S2) and indicated that the longest dimension of the crystal is along the  $b$  axis. We attempted various methods to optimize the synthesis, but the crystal size did not increase significantly further. Approximately 800 larger single crystals, with a total weight of  $\sim 10$  mg, grown using Eq. (2), were aligned along the  $b$  axis using GE varnish for magnetic property measurements. In sharp contrast, the aligned single-crystal sample exhibits no sharp ESR signals (see the main text), indicating the absence of quasi-free magnetic moments.

TABLE S2. The structural refinement of the single-crystal XRD data measured at 300 K. Positions and thermal parameters of H atoms were not refined and were kept consistent with Ref. [1]. Occupancy fractions were set to “1” for all atoms, following the methodology in Ref. [1].

Size	0.05×0.21×0.08 mm
Molar mass	385.6 g/mol
Space group	<i>Pnma</i>
<i>a</i>	13.8541(5) Å
<i>b</i>	6.0680(2) Å
<i>c</i>	6.2865(2) Å
Cell volume, <i>Z</i> = 1	528.49(3) Å <sup>3</sup>
Lu: <i>x, y, z</i>	0.41976(3),0.25,0.06365(6)
<i>U</i> <sub>iso</sub>	0.0032(1)
Cu: <i>x, y, z</i>	0.5,0,0.5
<i>U</i> <sub>iso</sub>	0.0061(3)
S: <i>x, y, z</i>	0.3070(2),0.75,0.2671(4)
<i>U</i> <sub>iso</sub>	0.0041(5)
O1: <i>x, y, z</i>	0.4175(5),0.25,0.433(1)
<i>U</i> <sub>iso</sub>	0.006(2)
O2: <i>x, y, z</i>	0.4620(4),0.9898(9),0.8042(8)
<i>U</i> <sub>iso</sub>	0.006(1)
O3: <i>x, y, z</i>	0.2028(6),0.75,0.310(1)
<i>U</i> <sub>iso</sub>	0.010(2)
O4: <i>x, y, z</i>	0.3629(6),0.75,0.466(1)
<i>U</i> <sub>iso</sub>	0.011(2)
O5: <i>x, y, z</i>	0.3294(4),0.947(1),0.1405(9)
<i>U</i> <sub>iso</sub>	0.016(1)
H1: <i>x, y, z</i>	0.3680,0.2500,0.5000
<i>U</i> <sub>iso</sub>	0.024
H2: <i>x, y, z</i>	0.4210,0.9480,0.7930
<i>U</i> <sub>iso</sub>	0.024
<i>h</i> range	−18 → 19
<i>k</i> range	−8 → 8
<i>l</i> range	−8 → 7
Reflections ( <i>I</i> > 0)	2484
Reflections ( <i>I</i> > 3σ( <i>I</i> ))	2427
<i>R</i> ( <i>F</i> ) ( <i>I</i> > 3σ( <i>I</i> ))	3.7%
<i>R</i> <sub>w</sub> ( <i>F</i> ) ( <i>I</i> > 3σ( <i>I</i> ))	4.5%

## II. NUMERICAL METHODS AND MODELS

Nearest-neighbor Dzyaloshinsky-Moriya (DM) interaction is symmetrically allowed in LuCu(OH)<sub>3</sub>SO<sub>4</sub>. Through a standard symmetry analysis, we find that the nearly Heisenberg Hamiltonian invariant under the *Pnma* space group symmetry of LuCu(OH)<sub>3</sub>SO<sub>4</sub> is given as,

$$\mathcal{H}_{\text{DM}} + \mathcal{H}' = -J_1 \sum_j \mathbf{S}_j \cdot \mathbf{S}_{j+1} + D \sum_j (-1)^{j+1} (S_j^x S_{j+1}^y - S_j^y S_{j+1}^x) + \mathcal{H}', \quad (3)$$

where  $\mathcal{H}' = J_2 \sum_j \mathbf{S}_j \cdot \mathbf{S}_{j+2} + J_{p1} \sum_{\langle j, jp1 \rangle} \mathbf{S}_j \cdot \mathbf{S}_{jp1} + J_{p2} \sum_{\langle j, jp2 \rangle} \mathbf{S}_j \cdot \mathbf{S}_{jp2} + \dots$  represents interactions beyond the nearest neighbors, encompassing next-nearest-neighbor (NNN) intrachain coupling  $J_2$ , interchain exchanges  $J_{p1}$  and  $J_{p2}$ , and so forth. In our exact diagonalization (ED) and stochastic series expansion (SSE) simulations, we employ the periodic boundary condition  $\mathbf{S}_j \equiv \mathbf{S}_{j+N}$ , where  $N$  is an even number of spins considered.

To estimate the strengths of  $J_2$ ,  $J_{p1}$ , and  $J_{p2}$ , we conducted density functional theory (DFT) calculations with a typical

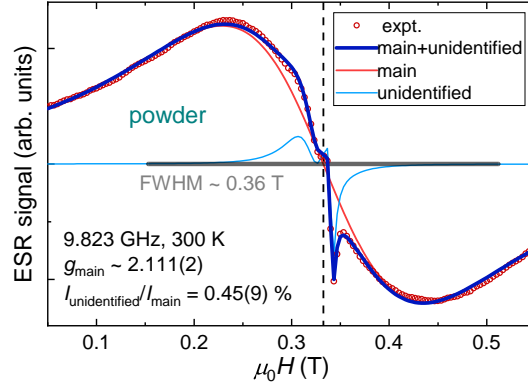


FIG. S3. Electron spin resonance (ESR) spectrum measured at 300 K on the powder sample ground from the smaller crystals [see Fig. S2(a)]. The observed sharp signals (unidentified) may originate from  $\sim 0.45\%$  of quasi-free-Cu<sup>2+</sup>-based impure phases. These sharp signals disappear in the ESR spectrum of the larger single crystals (see the main text).

TABLE S3. DFT calculations for exchange interaction energies using  $U = 5$  eV. The total and magnetic energies are relative values with respect to those of the fully ferromagnetic states, and the structural energy is independent of the magnetic structure.

Supercell	Positions of Cu	Magnetic structure	Total energy	Magnetic energy	Couplings
$1 \times 1 \times 1$	(0,0,0)(0,0.5,0) (0.5,0,0.5)(0.5,0.5,0.5)	$\uparrow\uparrow\uparrow$	0 K	0	
		$\uparrow\downarrow\downarrow$	100.7940 K	$2J_1$	$J_1 = 50.4$ K
		$\uparrow\uparrow\downarrow$	-0.2656 K	$-4J_{p2}$	$J_{p2} = 0.066$ K
$1 \times 2 \times 1$	(0,0,0)(0,0.25,0)(0,0.5,0)(0,0.75,0) (0.5,0,0.5)(0.5,0.25,0.5) (0.5,0.5,0.5)(0.5,0.75,0.5)	$\uparrow\uparrow\uparrow\uparrow\uparrow\uparrow$	0 K	0	
		$\uparrow\downarrow\uparrow\uparrow\downarrow\uparrow$	98.8146 K	$2J_1 - 4J_2$	$J_2 = 0.49$ K
$1 \times 1 \times 2$	(0,0,0)(0,0.5,0)(0.5,0,0.25) (0.5,0.5,0.25)(0,0,0.5)(0,0.5,0.5) (0.5,0,0.75)(0.5,0.5,0.75)	$\uparrow\uparrow\uparrow\uparrow\uparrow\uparrow$	0 K	0	
		$\uparrow\uparrow\downarrow\downarrow\downarrow\uparrow$	-9.9848 K	$-4J_{p1} - 4J_{p2}$	$J_{p1} = 2.4$ K

Coulomb repulsion of  $U = 5$  eV [7]. The DFT+ $U$  calculations were performed using the VIENNA AB INITIO SIMULATION PACKAGE (VASP) with the generalized gradient approximation [8–10]. We employed a  $4 \times 4 \times 4$  k-mesh, and residual forces were below  $0.003$  eV/Å in the fully optimized structure. The optimized structure remained unchanged in subsequent calculations of total energies for various magnetic structures and supercells. Electronic degrees of freedom relaxation were stopped when the total energy change and band structure energy change between two steps were both smaller than  $1 \times 10^{-7}$  eV = 1.2 mK. The precision was set to PREC = Accurate.

The strength of the nearest-neighbor exchange coupling monotonically decreases with increasing Coulomb repulsion  $U$ . DFT+ $U$  calculations suggest  $J_1 \sim 50$  K (see Table S3), roughly consistent with the experimental value obtained from the Curie-Weiss fits ( $J_1 \sim 65$  K). Therefore,  $U = 5$  eV is a suitable choice. Via DFT+ $U$  computations, we estimated  $J_2/J_1 \sim 1.0\%$ ,  $J_{p1}/J_1 \sim 4.8\%$ , and  $J_{p2}/J_1 \sim 0.1\%$ . The interactions beyond the nearest neighbors (terms in  $\mathcal{H}'$ ) are significantly smaller than the nearest-neighbor isotropic and DM couplings ( $J_1$  and  $D$  terms in  $\mathcal{H}_{DM}$ ).

We employed the SSE method within the general framework proposed in Refs. [11, 12]. To handle the antisymmetric DM interaction terms efficiently, we reduced the original DM model to the effective XXZ model through a unitary transformation (see the main text) [13]. While the transformation is mathematically strict, we carefully validated the reduced XXZ model by comparing it with finite-size ED calculations using the original DM model, as shown in Fig. S4. For chain lengths  $N$  less than  $\sim 30$ , ED/SSE simulations show evident finite-size effects at low temperatures of  $< 8$  K ( $\sim 0.1J_1$ ) despite the periodic boundary condition [see Fig. S4(b)], suggesting exotic ground-state properties of the spin-1/2 ferromagnetic XXZ chain system with long-distance unconventional entanglements. However, for  $N \geq 50$ , no finite-size effects are observed, and the 100-site ( $N = 100$ ) SSE calculations align well with integrable Bethe ansatz results at  $H \parallel z$  [see Figs. S4(b) and S5]. Therefore, we employed the 100-site SSE results for consistency throughout the main text. In practice, calculating the low-temperature specific heat exactly using the SSE method is challenging due to significant statistical errors [14]. The DFT+ $U$  calculations indicate a small strength for the NNN intrachain coupling, with  $J_2/J_1 \sim 1.0\%$  (see Table S3). Our many-body modeling further confirms the negligible

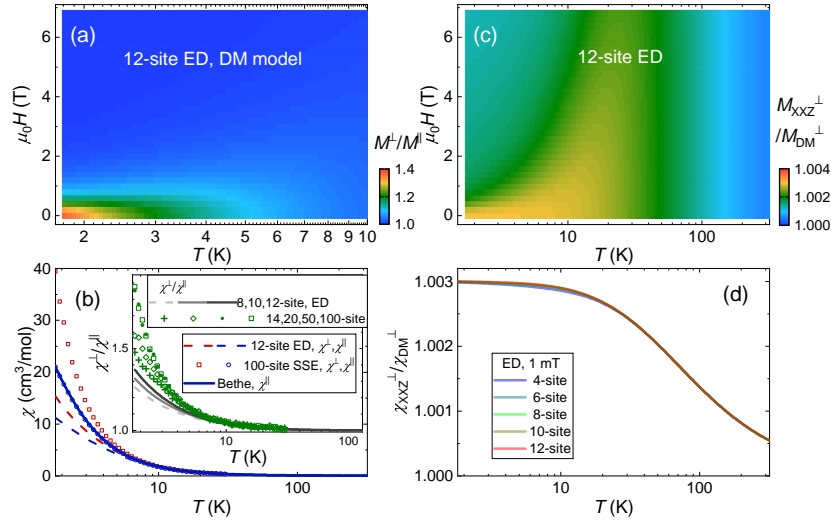


FIG. S4. Magnetization and susceptibilities calculated using ED, SSE, and Bethe ansatz methods, based on the DM and XXZ models,  $\mathcal{H}_{\text{DM}} = -J_1 \sum_j \mathbf{S}_j \cdot \mathbf{S}_{j+1} + D \sum_j (-1)^{j+1} (S_j^x S_{j+1}^y - S_j^y S_{j+1}^x)$  and  $\mathcal{H}_{\text{XXZ}} = -\sqrt{J_1^2 + D^2} \sum_j (S_j^x S_{j+1}^x + S_j^y S_{j+1}^y + \Delta S_j^z S_{j+1}^z)$ .  $J_1 = 65$  K and  $\Delta = 0.994$  (i.e.,  $D/J_1 = \sqrt{1/\Delta^2 - 1} = 0.11$ ) are used. (a) Anisotropy of magnetization ( $M^\perp/M^\parallel$ ) calculated using the 12-site ED method based on the DM model. “ $\perp$ ” and “ $\parallel$ ” represent the quantity with the magnetic field applied perpendicular and parallel to the  $z$  axis, respectively. (b) Calculated susceptibilities at  $\sim 0$  T ( $\chi^\perp$  and  $\chi^\parallel$ ). The inset shows  $\chi^\perp/\chi^\parallel$ . The DM model is used in the small-size ED calculations, whereas the XXZ model is used in the SSE and Bethe simulations. (c)  $M_{\text{XXZ}}^\perp/M_{\text{DM}}^\perp$ .  $M_{\text{XXZ}}^\perp$  and  $M_{\text{DM}}^\perp$  are 12-site ED calculated using the XXZ and DM models, respectively. (d)  $\chi_{\text{XXZ}}^\perp/\chi_{\text{DM}}^\perp$ .  $M_{\text{XXZ}}^\parallel \equiv M_{\text{DM}}^\parallel$  and  $\chi_{\text{XXZ}}^\parallel \equiv \chi_{\text{DM}}^\parallel$  are mathematically valid, and  $\chi_{\text{XXZ}}^\perp/\chi_{\text{DM}}^\perp$  ( $M_{\text{XXZ}}^\perp/M_{\text{DM}}^\perp$ ) is between 1 and 1.003, nearly independent of the chain length considered.

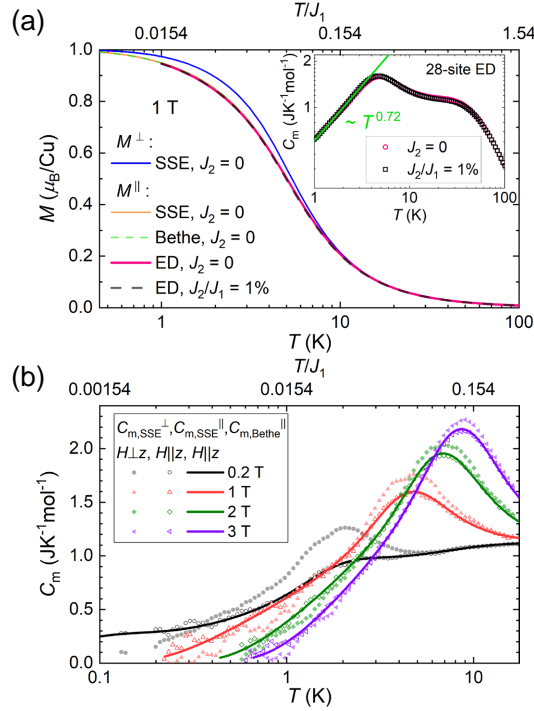


FIG. S5. (a) Magnetization calculated using the 100-site SSE, exact Bethe ansatz, and 28-site (Lanczos) ED [2] methods. The inset displays the ED specific heat, with the line showing the low- $T$  power-law behavior. The difference in quantities calculated with  $J_2 = 0$  and  $J_2/J_1 = 1\%$  is negligible, and finite-size effects are minimal for chain length  $N \geq 28$ . (b) Magnetic specific heat calculated using the 100-site SSE method, in comparison with the exact Bethe ansatz results. The Bethe method allows calculations only for quantities with the magnetic field applied parallel to the  $z$  axis [3–6]. The parameters  $J_1 = 65$  K and  $\Delta = 0.994$  are used.

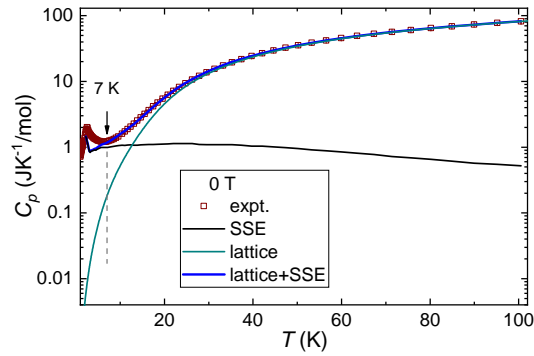


FIG. S6. Zero-field specific heat of  $\text{LuCu}(\text{OH})_3\text{SO}_4$ . The magnetic specific heat ( $C_{m,\text{SSE}}$ , black line) is calculated using the SSE method with the optimal parameter set I (see the main text). The blue line represents the fit to the experimental data (scatters) above 7 K, using the Debye-Einstein lattice function plus  $C_{m,\text{SSE}}$ .

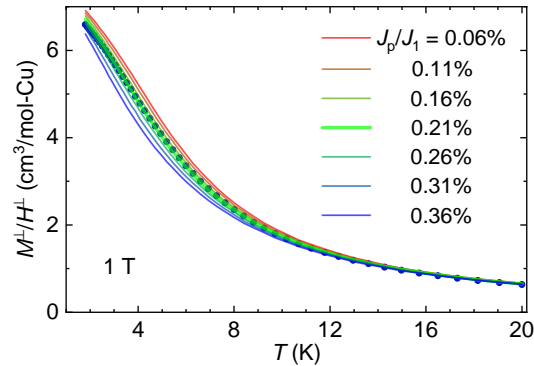


FIG. S7. Magnetization measured on the single-crystal sample with the magnetic field applied along the  $b$  axis ( $\mu_0 H^\perp = 1$  T). The colored lines show the SSE calculations with various  $J_p/J_1$  while keeping other parameters at their optimal values (see main text for details).

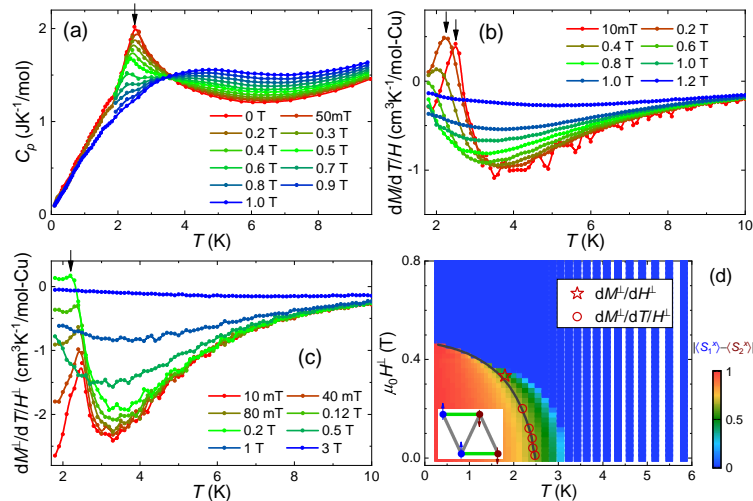


FIG. S8.  $B$ - $T$  phase diagram of  $\text{LuCu}(\text{OH})_3\text{SO}_4$ . (a) Specific heat measured on the powder sample at various applied fields. (b) The  $T$ -derivative magnetization ( $dM/dT/H$ ) measured on the powder sample at various applied fields. (c) The  $T$ -derivative magnetization ( $dM^\perp/dT/H^\perp$ ) measured on the single-crystal sample with magnetic fields applied along the  $b$  axis ( $H^\perp$ ). The arrows mark the critical temperatures  $T_c$ . (d) Interchain stripe-I order (lower inset) parameters calculated using the SSE method with a self-consistent mean-field treatment of interchain interactions (using the optimal parameters, as discussed in the main text). The critical field and temperatures obtained from the experimental  $dM^\perp/dH^\perp$  [see Fig. 4(b) in the main text] and  $dM^\perp/dT/H^\perp$  (see panel c) are displayed for comparison, and the thin line is a guide to the eyes.

impact of this  $J_2$  on both magnetization and specific heat, as illustrated in Fig. S5(a).

Using the optimal parameter set I, we calculated the SSE magnetic specific heat at 0 T,  $C_{m,SSE}$ , using a self-consistent mean-field treatment of interchain interactions (see the main text). Using  $C_{m,SSE} + C_{lattice}$ , we fitted the total specific heat of  $\text{LuCu}(\text{OH})_3\text{SO}_4$  measured at 0 T above  $\sim 7$  K (see Fig. S6). Here,  $C_{lattice}$  represents the lattice contribution of a standard Debye-Einstein function [2, 15], with the fitted parameters:  $\Theta_D = 97(1)$  K (wt. = 3),  $\Theta_{E1} = 133(1)$  K (wt. = 18),  $\Theta_{E2} = 283(3)$  K (wt. = 33), and  $\Theta_{E3} = 750(10)$  K (wt. = 102). Below  $\sim 7$  K,  $C_{lattice}$  becomes negligible compared to the magnetic specific heat  $C_m$ , with  $C_{lattice}/C_m < 0.1$  (see Fig. S6).

- 
- [1] H. J. Lu, K. Diefenbach, Z.-J. Li, H. L. Bao, X. F. Guo, J.-Q. Wang, T. E. Albrecht-Schmitt, and J. Lin, *Inorg. Chem.* **59**, 13398 (2020).
  - [2] J. Liu, L. Yuan, X. Li, B. Li, K. Zhao, H. Liao, and Y. Li, *Phys. Rev. B* **105**, 024418 (2022).
  - [3] M. Takahashi and M. Yamada, *J. Phys. Soc. Jpn.* **54**, 2808 (1985).
  - [4] P. Schlottmann, *Phys. Rev. Lett.* **54**, 2131 (1985).
  - [5] M. Takahashi, *World Sci.*, 299 (2001).
  - [6] M. Takahashi, *Czechoslov. J. Phys.* **53**, 1125 (2003).
  - [7] Y. Wang, S. Lany, J. Ghanbaja, Y. Fagot-Revurat, Y. P. Chen, F. Soldera, D. Horwat, F. Mücklich, and J. F. Pierson, *Phys. Rev. B* **94**, 245418 (2016).
  - [8] G. Kresse and J. Furthmüller, *Comp. Mater. Sci.* **6**, 15 (1996).
  - [9] G. Kresse and J. Furthmüller, *Phys. Rev. B* **54**, 11169 (1996).
  - [10] J. P. Perdew, K. Burke, and M. Ernzerhof, *Phys. Rev. Lett.* **77**, 3865 (1996).
  - [11] O. F. Syljuåsen and A. W. Sandvik, *Phys. Rev. E* **66**, 046701 (2002).
  - [12] A. W. Sandvik, *Phys. Rev. B* **59**, R14157 (1999).
  - [13] D. N. Aristov and S. V. Maleyev, *Phys. Rev. B* **62**, R751 (2000).
  - [14] A. W. Sandvik, *AIP Conf. Proc.* **1297**, 135 (2010).
  - [15] J. Liu, B. Liu, L. Yuan, B. Li, L. Xie, X. Chen, H. Zhang, D. Xu, W. Tong, J. Wang, and Y. Li, *New J. Phys.* **23**, 033040 (2021).